1-1-2013

Advanced Fuels Modeling: Evaluating the Steady-State Performance of Carbide Fuel in Helium-Cooled Reactors Using FRAPCON 3.4

Luke H. Hallman
University of South Carolina

ADVANCED FUELS MODELING: EVALUATING THE STEADY-STATE PERFORMANCE OF CARBIDE FUEL IN HELIUM-COOLED REACTORS USING FRAPCON 3.4

by

Luther Hallman Jr.

Bachelor of Science
Furman University, 2007

Submitted in Partial Fulfillment of the Requirements

For the Degree of Master of Science in

Nuclear Engineering

College of Engineering and Computing

University of South Carolina

2013

Accepted by:

Travis W. Knight, Major Professor

Elwyn Roberts, Reader

Lacy Ford, Vice Provost and Dean of Graduate Studies

DEDICATION

I dedicate this to my friends and family; I love you all.

ABSTRACT

Uranium carbide (UC) has long been considered a potential alternative to uranium dioxide (UO_2) fuel, especially in the context of Gen IV gas-cooled reactors. It has shown promise because of its high uranium density, good irradiation stability, and especially high thermal conductivity. Despite its many benefits, UC is known to swell at a rate twice that of UO_2. However, the swelling phenomenon is not well understood, and we are limited to a weak empirical understanding of the swelling mechanism.

One suggested cladding for UC is silicon carbide (SiC), a ceramic that demonstrates a number of desirable properties. Among them are an increased corrosion resistance, high mechanical strength, and irradiation stability. However, with increased temperatures, SiC exhibits an extremely brittle nature. The brittle behavior of SiC is not fully understood and thus it is unknown how SiC would respond to the added stress of a swelling UC fuel.

To better understand the interaction between these advanced materials, each has been implemented into FRAPCON, the preferred fuel performance code of the Nuclear Regulatory Commission (NRC); additionally, the material properties for a helium coolant have been incorporated. The implementation of UC within FRAPCON required the development of material models that described not only the thermophysical properties of UC, such as thermal conductivity and thermal expansion, but also models for the

swelling, densification, and fission gas release associated with the fuel's irradiation behavior.

This research is intended to supplement ongoing analysis of the performance and behavior of uranium carbide and silicon carbide in a helium-cooled reactor.

TABLE OF CONTENTS

LIST OF TABLES

LIST OF FIGURES

List of Abbreviations

AGR ..... Advanced Gas Reactor

EM2 ..... Energy Multiplier Module

GA ..... General Atomics

GIF ..... Generation IV International Forum

GFR ..... Gas-Cooled Fast Reactor

GT-MHR ..... Gas Turbine Modular Helium Reactor

HTGR ..... High Temperature Gas Reactor

LFR ..... Lead-Cooled Fast Reactor

LOCA ..... Loss of Coolant Accident

LWR ..... Light Water Reactor

MOX ..... Mixed Oxide

MSR ..... Molten Salt Reactor

NaCl ..... Sodium Chloride

NRC ..... Nuclear Regulatory Commission

SCWR ..... Supercritical-Water-Cooled Reactor

SiC ..... Silicon Carbide

UC ..... Uranium Carbide

UO_2 ..... Uranium Dioxide

VHTR ..... Very High Temperature Reactor

CHAPTER I

INTRODUCTION

In July 2001, an international task force was chartered with the purpose of developing a nuclear reactor technology that would lead us into the future. The Generation IV International Forum (GIF), as they became known, identified four primary areas to focus their research efforts; the next generation of nuclear technology should demonstrate enhanced safety, reduced financial investment, nominal nuclear waste generation, and increased proliferation resistance [1].

After a thorough examination of nearly 100 different designs, six conceptual technologies were selected for further research and development; the target is for a model of each to be in operation by the year 2030. The systems chosen include a gas-cooled fast reactor (GFR), very-high-temperature reactor (VHTR), supercritical-water-cooled reactor (SCWR), sodium-cooled fast reactor (SFR), lead-cooled fast reactor (LFR), and molten salt reactor (MSR) [2].

One design in particular, the gas-cooled fast reactor, was chosen because it demonstrated all of the desirable traits necessary for a next gen design. Unique to the GFR design is a fast-neutron spectrum, an inert helium coolant, and a closed fuel cycle. Because they operate at an extremely high temperature (~850˚C), they are well suited for not only electricity generation but process heat applications as well. Additionally,

because they employ a direct Brayton cycle, they are expected to operate with efficiency one and half times that of a conventional light water reactor (LWR) [1, 2].

Beyond these basic characteristics, there are a number of variants of the GFR design. Multiple fuel types & configurations have been considered including composite ceramics, advanced fuel particles, and ceramic-clad elements in prismatic block, pin, or plate geometries. Above all, it is absolutely essential that the fuel is capable of performing in the harshest of thermal environments and exhibits excellent fission product retention [3].

The motive for utilizing a GFR cannot be narrowed to just one reason. In fact, the motivation stems from multiple advantageous characteristics. Compared to today's LWR, fast spectrum reactors offer a much more efficient use of fuel. Moreover, GFRs are capable of burning spent fuel or depleted uranium without the need for reprocessing. In doing so, the waste generated is not only greatly reduced, but we now have a disposal method for current 'waste' supplies. Additionally, GFR's use of helium coolant reduces a number of concerns. Chemically inert, helium offers the ability to operate at high temperatures without concern of corrosion. Furthermore, a single-phase coolant eliminates boiling [1, 3].

Despite a number of advantages, the gas-cooled fast reactor is not without its shortcomings. However, a strong understanding of the GFR's inadequacies and limitations can be seen as a positive. The primary area of concern for a gas-cooled fast reactor is in a LOCA scenario. The high power density makes for an extremely hot core, and coupled with the coolant's low thermal inertia makes for an area of concern [1].

And given the novelty of the design, there are a number of challenges yet to be solved, primarily in the materials category. The issue of determining a suitable core structural material has yet to be decided. Moreover, an appropriate fuel – cladding combination must be settled upon [4].

One company in particular has taken special interest in the GFR design: General Atomics (GA). GA is no stranger to helium-cooled reactors, with a resume that includes Dragon, Peach Bottom, and Fort St. Vrain. Their most recent design, the Energy Multiplier Module (EM2), is a redesign of their popular gas turbine modular helium reactor (GT-MHR) [5].

General Atomics has taken a unique approach to the GFR design. Unlike a conventional LWR or GFR design, GA's design can be fabricated offsite, transported via rail- or roadway, and assembled on-site using traditional engineering methods. In other words, it is completely modular. And because of this, the capital costs and average cost per kW-hr are reduced by as much as 30% (compared to a typical LWR) [5].

Each EM2 unit is comprised of two modules equating to 480MWe; one module is a quarter size of an LWR. The core design is 40 feet long and 16 feet in diameter. Figure 1.1 depicts one module (rated at 240MWe); the middle unit is the reactor core itself, and to the left and right of it are the heat removal system and the gas turbine system respectively. The entire unit is placed below ground, and features a natural convection core cooling system for passive safety [5, 6].

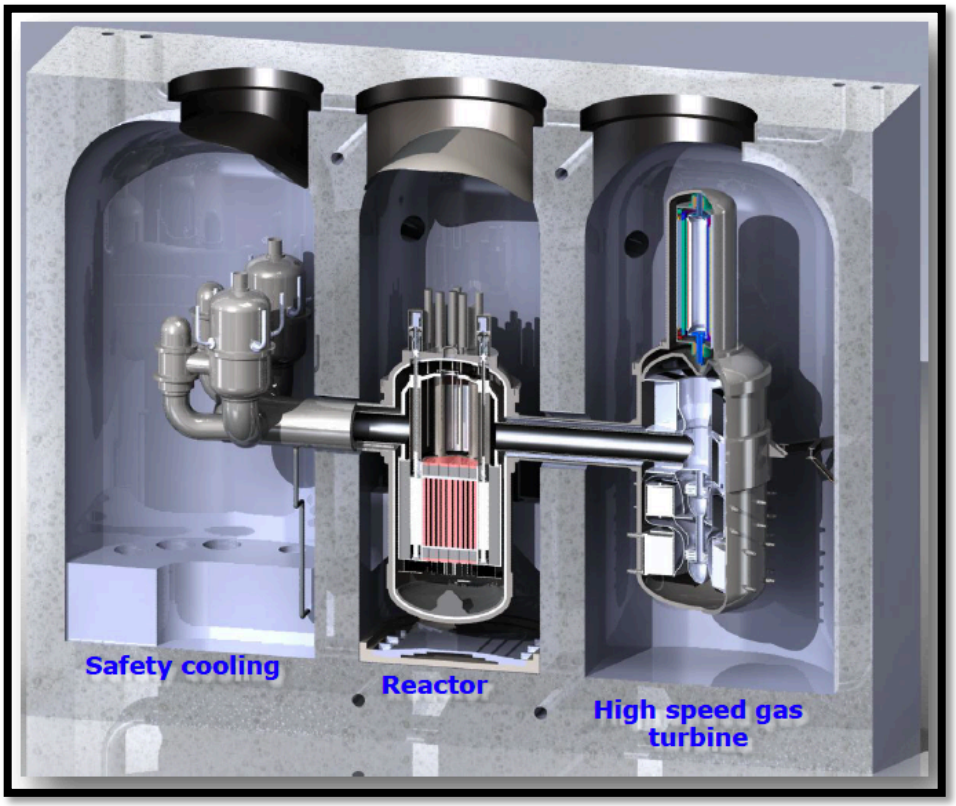

Figure 1.1 One 240MWe module of an EM2 unit [6]

The design has the ability to burn spent fuel, and dispose of much of the wastes in the process. By current estimates, in the US alone there is enough spent fuel to power 3000 units. One serious drawback of current reactors is their inability to adequately utilize the capability of the fuel without reprocessing. Spent fuel contains more than 95% of its potential. EM2 has the ability to use spent fuel from LWRs or depleted uranium. Because of this, the need for long-term repository is greatly reduced [5, 6].

GA has proposed an all-ceramic core consisting of a uranium carbide fuel clad in a silicon carbide composite. UC was chosen for its extraordinarily high thermal conductivity and high fissile density [7]. A more thorough review of the performance and design parameters can be seen in Table 1.1.

Table 1.1 EM2 design parameters [30]

Reactor power	500 MW thermal
Fuel material	Uranium carbide
Clad/structure material	Silicon carbide
Coolant material	Helium
Cycle length	32 years
Average fissile content	6.1 wt%
Fuel loading	
Uranium	42.8 t
^{235}U	2.6 t
Fuel discharged	
Heavy metal	36.7 t
Uranium consumed	23%
Excess reactivity	2.0% δk
Peak/average burnup	285/135 GWd/t
Peak/average power density	165/58 W/cm^3
Peak/average fast fluence (>0.1 MeV)	$7.9/3.7 \times 10^{23}$ n/cm^2
System pressure	13.3 MPa
System pressure (depressurized)	0.45 MPa
Core pressure drop	25 kPa
Core inlet temperature	549°C
Core outlet temperature	850°C

Using GA's design as inspiration, the proposed research investigates UC and SiC as potential fuel and cladding replacements in a helium cooled environment. Given that a true gas-cooled fast reactor has never been built, many questions remain unanswered, especially with regards to fuel behavior and in-pile performance.

It is our intention to model the steady-state interaction between UC and SiC by modifying FRAPCON 3.4, the preferred fuel performance code of the U.S. Nuclear Regulatory Commission (NRC). By altering properties of the code, we hope to develop a model that closely depicts UC's behavior and its resulting interaction with SiC cladding in a helium-cooled environment.

Although the concept of employing a carbide fuel isn't new, our understanding of its behavior is limited (its swelling in particular). Still, its known benefits are hard to ignore. Like UO_2, uranium carbide has a relatively high melting point and irradiation

stability; but what really sets UC apart is its considerably higher thermal conductivity and fissile density (and burnup potential). Despite its upside, there is one issue plaguing the fuel: swelling. Uranium carbide is known to swell at rate twice that of its uranium dioxide counterpart. Currently, the phenomenon is not well understood, and we are limited to a weak empirical understanding of the swelling mechanism.

An advanced fuel such as UC requires a cladding that can withstand the increased temperature and burnup. The suggested material, silicon carbide, is a ceramic that demonstrates a number of desirable properties. Among them are an increased corrosion resistance, high mechanical strength, and a reasonable thermal conductivity. However, with increased temperatures, SiC exhibits an extremely brittle nature, and it is not well understood how such a material would respond to the added stress of a swelling fuel (i.e. UC).

Given that a GFR has yet to become operational, and that data on the materials in question is limited, there is a relative degree of uncertainty. The goal of the research is to better understand the behavior of the uranium carbide and silicon carbide interaction by developing a working steady-state computer model. Moreover, the research is intended to supplement the research already in progress for Generation IV reactor designs.

CHAPTER II

A REVIEW OF URANIUM CARBIDE

Carbides have long been considered a potential alternative to uranium dioxide (UO_2) fuel, especially in Gen IV designs. More specifically, they have shown promise because of their high uranium density, good irradiation stability, strong retention of fission products, and elevated thermal conductivity [8]. As such, carbides are well suited for high temperature applications where higher power ratings and breeding capabilities are desired, i.e. fast gas reactor designs.

Properties of particular interest include the: stoichiometry, structure, thermophysical properties, and irradiation behavior. Given the limited availability of data on uranium carbide, the scope of the study may extend to mixed carbides, i.e. (U,Pu)C. However, replacing a small percentage (< 20%) of uranium with plutonium should not significantly alter the properties.

2.1 STOICHIOMETRY AND STRUCTURE

The uranium-carbon constitutional diagram is composed of three compounds: UC, UC_2, and U_2C_3. Stoichiometric uranium monocarbide is 4.8% carbon by weight, has an invariant composition in the temperature range of interest, and crystallizes in the FCC NaCl structure [9]. It has the highest density of the three at 13.63 g/cm^3.

UC_2 has a FCC fluorite structure at higher temperatures, and transforms into a body-centered tetragonal structure at 1820˚C. The phase is retained as a metastable form

in material that has been rapidly been cooled from melting temperatures. Additionally, it is known to transform into U_2C_3 above 1400˚C while under stress; however, it can't be directly produced by casting or compaction of powders. At temperatures higher than 1800˚C, it decomposes back into UC and UC_2 [10].

Figure 2-1 is the equilibrium phase diagram of uranium carbide. According to Hubert, the UC phase is a line compound at temperatures below 1400K, but attains a wider phase field with increased temperatures. This begins initially on the hypostoichiometric side, however around 1900K the cubic phase widens toward the hyperstoichiometric side until it covers a range of 0.90 < C/U < 2.0 [11]. As will be shown later, the stoichiometry can have a large influence on the behavior of uranium carbide.

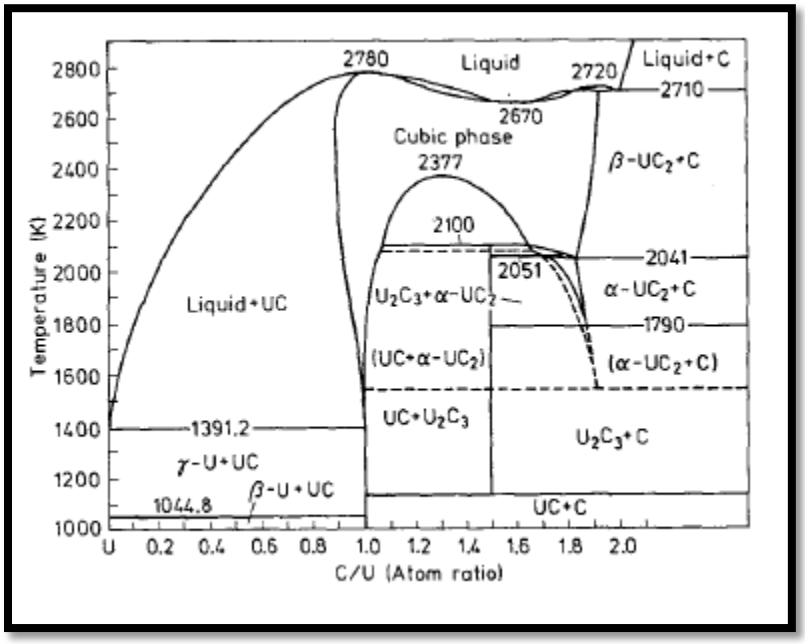

Figure 2.1 U-C Phase Diagram [12]

Rough and Dickerson suggested that hypostoichiometric UC may be undesirable from a radiation damage standpoint; the radiation-induced growth of the uranium area could lead to internal stresses and cracking [12].

In the most general terms, porosity, density, and grain size are the primary fuel structure properties that determine a fuel's performance parameters including resistance to swelling and creep, fission gas production and release, and fuel pellet cracking. And in large, the techniques employed during fabrication dictate these properties [13].

As noted, the manufacturing process is integral for controlling the structural properties. Nickerson noted that arc melting produces a high density (98-99%), large grain (100 mm) and low impurity (100-200 ppm) structure, whereas sintering creates a lower density (92-96%), smaller grain (10-15 mm), and higher impurity (0.3%) fuel. While each method has distinct advantages, ultimately the chosen manufactured method is based on the fuels application, as well as the feasibility and consistency of the process.

High-density (96 – 99%TD) carbides retain a higher amount of fission gases than their lower-density (77-91%) counterpart. Pores are advantageous in that they allow for individual grains to swell by supplying vacancies to accommodate fission gases generated in the matrix. And in doing so, the swelling rate is reduced lessening the potential for fuel-clad mechanical interaction [13].

Although the data on stoichiometric uranium carbide's density is readily available, it is unclear as to how it changes with increased burnup [13]. Additionally, alloying and buffering agents can further reduce this value. The fuel's lifetime is strongly determined by its density.

2.2 Thermophysical Properties

Because the scope of the research is focused on the steady-state performance of uranium carbide, the primary thermal properties of interest are thermal conductivity and thermal expansion. Several factors can have an influential effect on these properties including fabrication method, chemistry, microstructural and macrostructural effects, irradiation effects, and experimental method of property measurement [14].

2.2.1 Thermal Conductivity

UC's relatively high thermal conductivity is a fundamental reason for suggested use in advanced reactor designs. A much higher power density is achievable without increased risk of melting the fuel. In fact, uranium carbide operates with a flatter temperature gradient than that of UO_2 [in similar conditions] allowing for increased burnups, all while improving operating safety margins.

In carbides, phonon and electron motion are the primary modes of heat transition; at high temperatures electronic motion dominates. Additional factors to consider in regards to the thermal conductivity are temperature, porosity, alloy composition, burnup, and fission gas content [15].

Most research to date has produced models that are temperature and porosity dependent. Using such equations on fuels of higher burnups can lead to unsatisfactory results. A equation that incorporates alloy composition, burnup, and fission gas release would yield more accurate results; however, no such relation exists [15].

Washington reviewed the data of 15 separate studies and was able to derive an expression for 100% dense stoichiometric uranium carbide. His studies indicated that conductivity increases linearly from 20 to 22 W/m˚C in a temperature range of 500 to 2000˚C. Also reviewed were the effects of stoichiometry; however, from his analyses, it

was determined that the effects of stoichiometry were very speculative. He offered a tentative correlation for a hypostoichiometric material, but concluded that it was impossible to do so for a hyperstoichiometric material.

Additionally, Washington examined the effects of porosity on thermal conductivity; he concluded that a quantitative separation of effects was not possible and that a true porosity correlation would be temperature and pore-shape dependent. Although unable to determine a precise correction, he did suggest a conservative estimate that could be used for all compositions.

Lastly, the effects of oxygen impurity were reviewed; Washington's findings were based on the works of six independent studies. In general, it is evident that thermal conductivity is decreased by oxygen impurity with the greatest effects observed below 1000˚C. However, he concluded that with the available data, separation of the effects of stoichiometry and impurities wasn't possible. Tentatively, he offered an expression for the effects of oxygen impurities [17].

Table 2.1 Washington's suggested thermal conductivity equations

$k\ (W/m^{\circ}C) = 20.0 + 1.30 \times 10^{-3} (T - 500)$	*[500 ≤ T ≤ 2000 ˚C] 100% TD stoichiometric*
$k\ (W/m^{\circ}C) = 16.0 + 3.40 \times 10^{-3} (T - 500)$	*[500 ≤ T ≤ 2000 ˚C] hypostoichiometric (4 wt% C)*
$k\ (W/m^{\circ}C) = 16.0 + 3.40 \times 10^{-3} (T - 500)$	*[500 ≤ T ≤ 2400 ˚C] 5 at% Oxygen*
$k\ (W/m^{\circ}C) = 14.0 + 4.50 \times 10^{-3} (T - 500)$	*[500 ≤ T ≤ 2400 ˚C] 7.5 at% Oxygen*
$k_p = k\ [(1-P)/(1+P)]$	*P = porosity fraction*

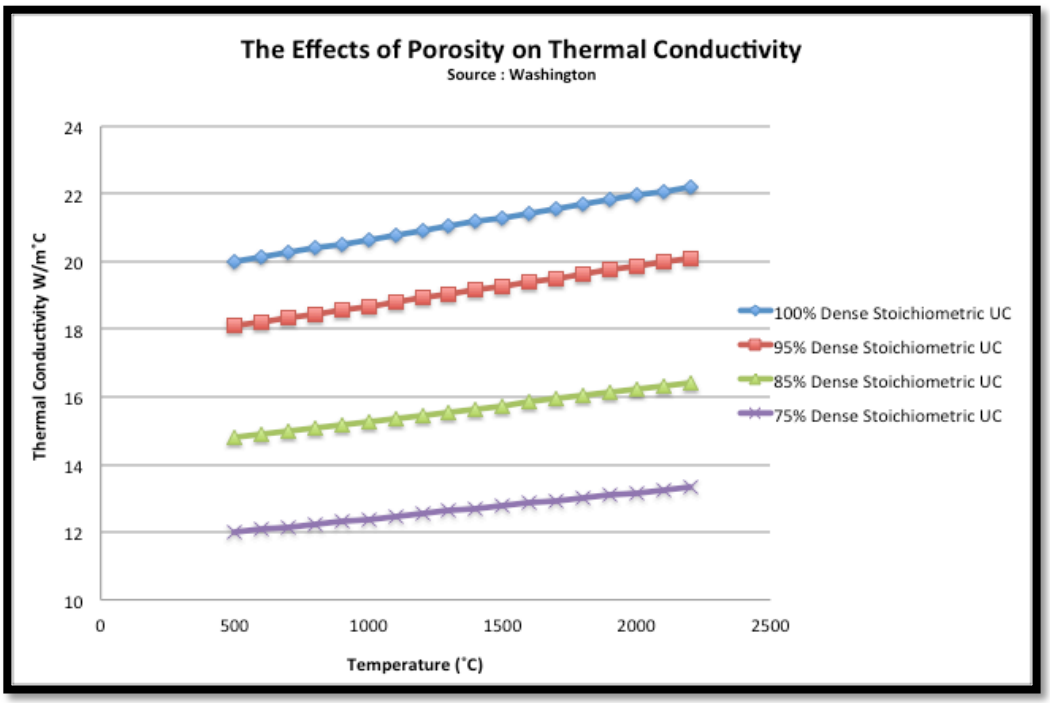

Figure 2.2 The effects of porosity on thermal conductivity in uranium carbide

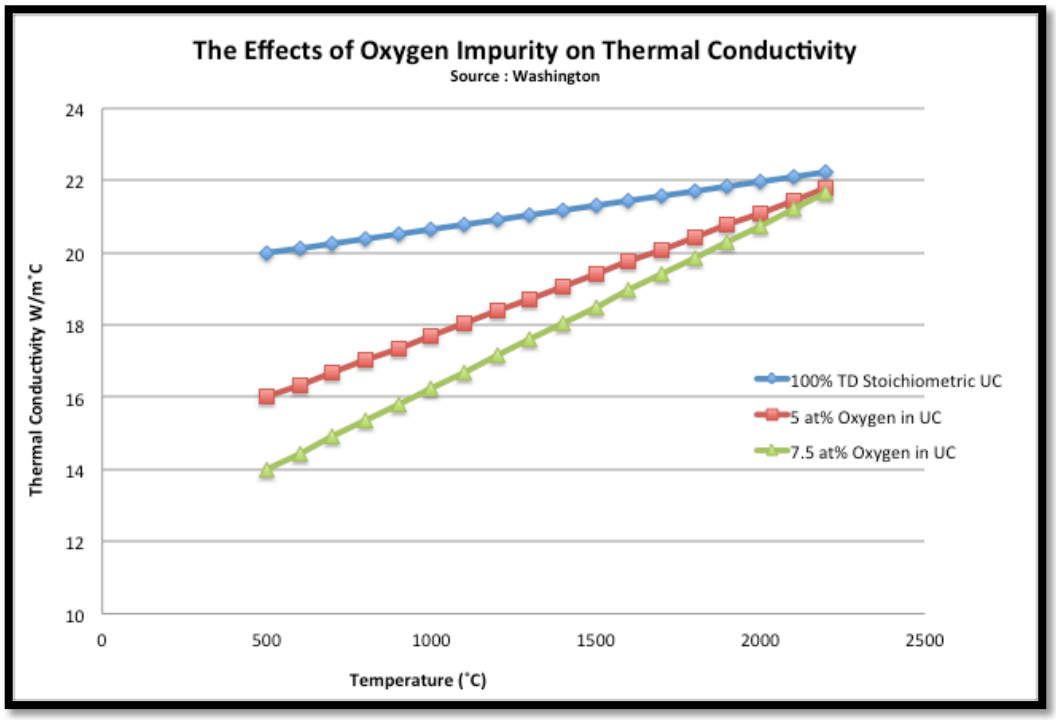

Figure 2.3 The effects of oxygen impurity in uranium carbide

In one of the more ‘recent’ studies, Lewis and Kerrisk assessed the data of 23 different reports. Several materials, stoichiometries, and porosities were reviewed before determining best-estimate equations.

The reported data suggests a wide range for carbide’s thermal conductivity over the temperature range studied. In large, the variability can be attributed to many factors including the: concentration of carbon, concentration of second phase dicarbide and sesquicarbide, presence of oxygen and nitrogen, porosity, and addition of nickel through the sintering process. Given the limited data, a quantitative evaluation of every individual factor wasn’t feasible. However, several equations were suggested based on the present data available [14].

Given the experimental data available, the effects of porosity could not be qualitatively assessed; this is not surprising as Washington came to a similar conclusion. However, Lewis and Kerrisk suggested a porosity correction factor (Figure 2-5); the disparity between the two suggested factors will need to be reviewed further.

Like Washington, they considered the effect of oxygen impurities, and concluded that they do not significantly affect thermal conductivity below 2500ppm. In higher quantities though, oxygen can significantly reduce thermal conductivity. Lastly, the effects of nitride impurities were discussed; data was too inconclusive to draw any concrete correlations, but based on the limited nitride data, the general consensus is that the thermal conductivity would be lowered [14]. See Table 2.5 for a complete review of Lewis and Kerrisk’s suggested correlations.

Table 2.2 Suggested thermal conductivities found in Lewis & Kerrisk report

$k\ (W/m^{\circ}C) = 21.7 - 3.04\times10^{-3}T + 3.61\times10^{-6}T^2$	*[50 ≤ T ≤ 700 ˚C]* *100% TD UC*
$k\ (W/m^{\circ}C) = 20.2 + 1.48\times10^{-3}\ T$	*[700 ≤ T ≤ 2300 ˚C]* *100% TD UC*
$k\ (W/m^{\circ}C) = 3.24 + 6.92\times10^{-3}T$	*[300 ≤ T ≤ 2000 ˚C]* *100% TD UC_2*
$k\ (W/m^{\circ}C) = 6.58 + 5.63\times10^{-3}T$	*[25 ≤ T ≤ 1750 ˚C]* *100% TD U_2C_3 + 15 vol% UC*
$k\ (W/m^{\circ}C) = 21.3 - 4.66\times10^{-3}T + 2.40\times10^{-6}T^2$	*[100 ≤ T ≤ 2300 ˚C]* *100% TD UC (0.3 wt% oxygen)*
$k\ (W/m^{\circ}C) = 12.4 + 2.73\times10^{-3}T + 6.55\times10^{-7}T^2$	*[100 ≤ T ≤ 2300 ˚C]* *100% TD UC (2.0 wt% oxygen)*
$k_M = k_{TD}\ (1-P)$	*P = porosity fraction*

In Figures 2.6 and 2.7, the thermal conductivity relationships from above are plotted. Of particular importance is that Lewis and Kerrisk predict a slightly higher thermal conductivity for 100% theoretical density carbide as that of Washington. Additionally, the porosity correlation as suggested by Lewis has less of an impact on the thermal conductivity. This is especially evident with increasing porosity; for example, a porosity of 15% reduces the thermal conductivity by the same value (15%). However, as suggested by Washington, 15% porosity reduces thermal conductivity by 26%. [14,17]

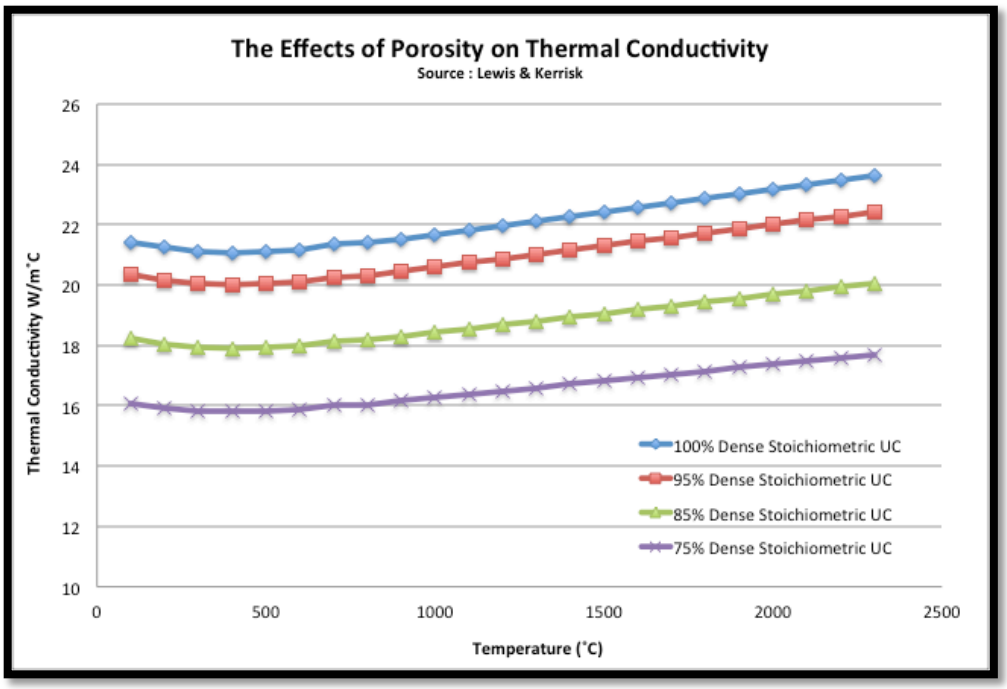

Figure 2.4 Effects of porosity on conductivity as suggested by Lewis

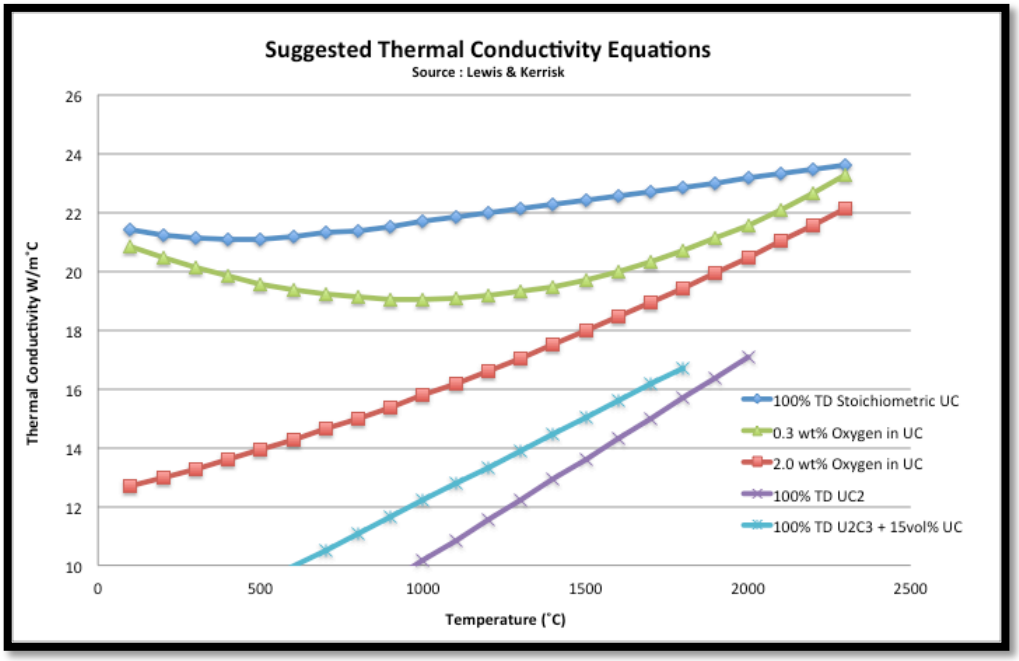

Figure 2.5. Thermal conductivity relationships as suggested by Lewis

2.2.2 THERMAL EXPANSION

Thermal expansion in uranium carbide is of interest in two distinct temperature regions: (a) $300K < T < 0.6T_{melt}$ for normal reactor operation and (b) at $T > 0.6T_{melt}$ for off normal or accident situations. Since the steady-state performance of uranium carbide is the primary focus in this study, the data will be limited to temperatures in normal operating range [11].

The coefficient of linear expansion is required for calculations of the thermoelastic stresses in the radial temperature gradient. Moreover, it is one of the primary components that govern the width and thermal resistance of the fuel-cladding gap.

Data on uranium carbide's coefficient of thermal expansion is readily available, and for the most part tends to agree with one another. Given the high temperatures under which the fuel is expected to perform, a strong knowledge of uranium carbide's thermal expansion is necessary. Factors to consider include temperature, composition, stoichiometry, and the manufacturing process [15].

Table 2.3 details the available experimental data. When possible, the temperature range, stoichiometry, or manufacturing process was noted. Additionally, Table 2.4 is a compilation of expansion expressions, which were derived from experimental data to best estimate the coefficient of thermal expansion as a function of temperature.

Table 2.3 UC thermal expansion data

Temp (˚C)	α (10^{-6}/˚C)	Notes	Reference
1000 1500 2000	10.67 11.79 13.05		Krikorian [18]
1000 1000	11.3[a] 11.8[b]	[a]4.8 wt% carbon content [b]5.2 wt% carbon content	Crane [19]
1000 1600 2000	11.2 12.0 12.4	Averaged from 4.9, 5.04, 5.05 wt% carbon content specimen.	Mendez [20]
1000 1500 2000 2400	12.6 13.7 14.7 15.5	Averaged from 5.01 and 5.10 wt% carbon content specimen.	Richards [21]
400 600 800 1000 1200 1400	10.6 11.3 12.0 12.2 12.4 12.6	Arc cast	Nickerson [13]
400 600 800 1000 1200	8.1 9.1 10.0 10.8 11.3	Sintered	Nickerson [13]

Table 2.4 Thermal expansion coefficient expressions

Coefficient Expression (1/T)	Notes	Reference
8.9622E-6 + 3.2642E-9T – 6.1191E-13T^2	T in K	Politis [11]
9.3877E-6 + 2.3772E-9T	T in K	Mendez [11]
9.3467E-6 + 2.35128E-9T	T in K	De Crescente [11]
1.007E-5 + 1.17E-9T	T in ˚C	Elbel [15]

In Figure 2.6, all the experimental data from above, as well as the coefficient of thermal expansion expressions, are plotted. Because the data is limited, the effects of manufacturing process and stoichiometry are not considered. Furthermore, they are not taken into account in the equations above, i.e. all data is used to derive the expression. In general, the expressions tend to agree well with the experimental data, as well as with one another. Of the four, Elbel's equation tends to predict the highest thermal expansion coefficient, especially in the temperature range of interest.

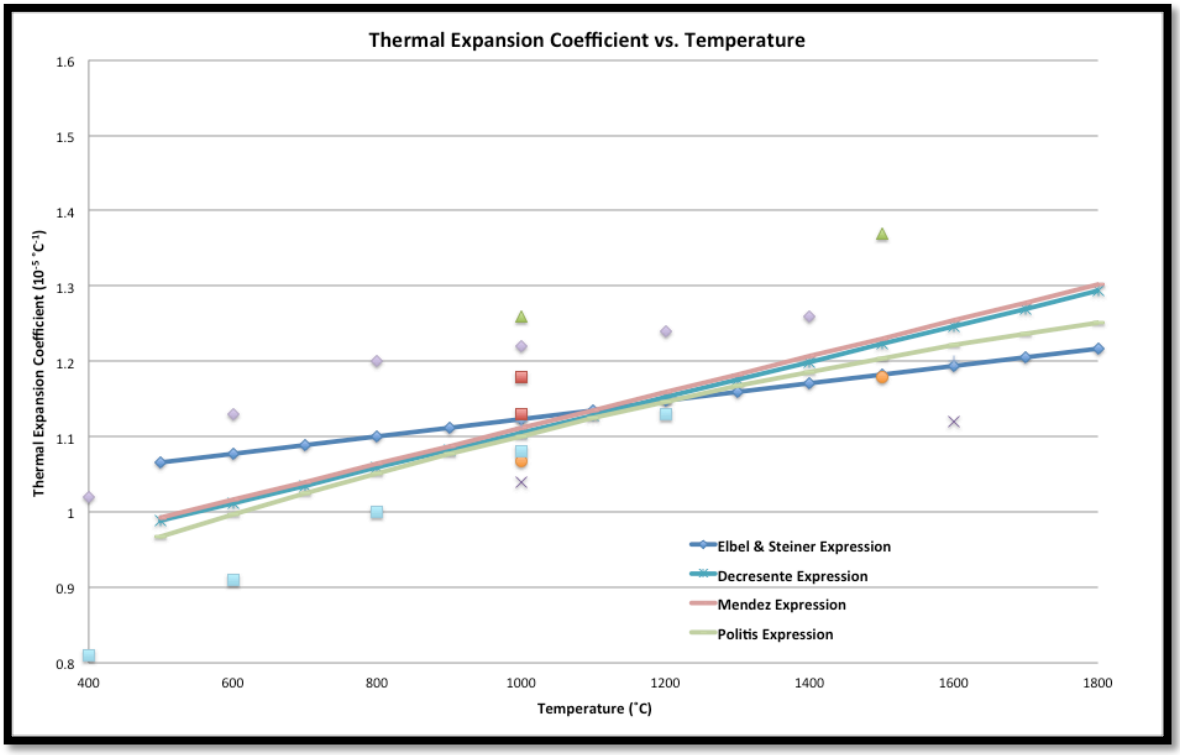

Figure 2.6 Uranium carbide thermal expansion coefficients

Based on the experimental data, stoichiometric carbides behave as one might at expect with an increasing curve gradient with increasing temperature. However, unstoichiometric fuels behaved in a more divergent manner. This may be attributed to phase changes of the free uranium at grain boundaries [15].

2.3 Irradiation Behavior

For carbide fuel pins, in a fast reactor environment, strong mechanical interaction between fuel and cladding is often inevitable, largely because carbides can be expected to experience a relatively large amount of dimensional change. The resultant cladding strain is dependent on the swelling [attributed to both solid & gaseous fission products], irradiation-induced densification, and irradiation-induced creep of the UC fuel [22].

2.3.1 Swelling

Swelling can be attributed to the buildup of gaseous and solid fission products. The fraction of solid fission, which accumulates in the fuel, is dependent on burnup, whereas the retention of gaseous fission products is strongly dependent on local structure and temperature. Lambert noted that up to 60% of the fission gases generated within uranium carbide are retained in the matrix. As shown earlier, UC's thermal conductivity results in a much flatter temperature profile across the fuel. And because fission gas release is heavily dependent on temperature, a relatively large amount of the gases will remain in the fuel, resulting in this increased swelling rate [13,15].

The fundamental factors that influence swelling are temperature, burnup, stoichiometry, alloy composition, porosity, grain size, and neutron flux [15]. Because there are a large number of influential effects, a comparison of different experiments can be difficult. However, generalities about the swelling behavior of carbide can be made.

Overall, the swelling behavior of a high-density fuel (> 90%) differentiates itself from that of a low-density fuel (77 – 90%) because of its decreased capacity to swell into the pores. Increased temperature and burnup will increase the swelling rate. Hypostoichiometric fuels will swell more quickly than that of a stoichiometric one because the free uranium forms a lower melting eutectic (thereby lowering resistance to

swelling). Impurities act to reduce the swelling rate because they hinder gas diffusion and restrict the formation/motion of gas bubbles. Excess carbon content acts to do the same [15].

Irradiation tests were performed by W. Dienst at Kernforschungszentrum Karlsruhe (KfK) in order to determine the behavior of helium bonded (U,Pu)C fuel under irradiation. In particular, he analyzed the swelling of mixed carbides (MC) in two situations: free swelling and swelling under cladding restraint. More specifically, special attention was given to temperatures at or below 1200˚C (~ ½ melting point); above that, the fuel was considered unable to bear the mechanical loads resulting from the cladding restraint.

Below 1000˚C, a free swelling rate of about 1.5 vol% per at% burnup was observed. And in general, temperatures below 850˚C resulted in a 1.45 vol% per at% burnup. The general behavior of the tested fuel pins ranged from 1.2 and 1.7 vol% per at% burnup. A resulting linear expression (for these lower temperatures) was determined in order to express the burnup dependence of the free swelling:

$$\delta V/\Delta B = (1.17 + 0.18B) \text{ vol\% per at\% burnup}$$

where B is the burnup in at% (U+Pu).

In addition, Dienst performed studies of the swelling rate of mixed carbides while under cladding restraint. He predicted that swelling of the fuel is largely dependent on the temperature of the outer most region of the fuel. Available void volumes can accommodate the hotter inner regions (due to thermal creep plasticity). As such, he predicted that the swelling rate would be comparable to that of lower temperature (<1000˚C) free swelling rates. Using the cladding strain (experimentally determined) and

the creep behavior of the fuel, Dienst calculated an actual integral swell rate of (U, Pu)C under cladding restraint. The resulting swelling rates of (U, Pu)C fuel under cladding restraint ranged from 1.0 to 1.5 vol% per at% burnup [22].

Nickerson assessed numerous studies and made several observations regarding the swelling trends of carbides. In general, he noted that hypostoichiometric UC swelled the most, while hyperstoichiometric uranium carbides with 0.1wt% nickel swelled the least. He observed a 1.6 to 3.0% density decrease per 10^4 MWd/MTU (approximately 1.0 at% burnup) for stoichiometric and hyperstoichiometric carbides. In order to accommodate such swelling, Nickerson recommended a 20% volume void (based on a 10 at% burn-up); this can be achieved with a smeared fuel density of 84.5% TD. Lastly, Nickerson noted that breakaway swelling in stoichiometric UC onsets at 1050˚C, where as in hyperstoichiometric UC, it onsets around 1375˚C [13].

Preusser developed an empirical model to describe the swelling rate of uranium carbide, which is based on experimental data only. The model considers swelling due to both solid and gaseous fission products; it is dependent on porosity, temperature, and burnup. Additionally, open and closed gap regimes are accounted for through the use of contact pressure.

In the case of hard contact between fuel and cladding, the swelling rate is taken to be at a minimum: 0.4667 vol% per at% burnup. This value includes the effects of hot pressing as well. The maximum rate of swelling was taken to be a high-density fuel, without cladding contact: 2.1780 vol% per at% burnup (at a temperature below which gas bubble swelling occurs ~ 700˚C). Above this temperature, additional swelling rate due to gas swelling is taken into account [15]. Below is Preusser's proposed model:

Table 2.5 Carbide swelling model

$\Delta V/V = 0.4667 + 1.711 \cdot f(P,pc)$	Up to 700˚C
$\Delta V/V = 0.4667 + 1.711 \cdot f(P,pc) + [(6.412 - 0.0198T + 0.152x10^{-4}T^2) \cdot f(BU) \cdot f(P,pc)]$	Above 700˚C
$\Delta V/V = 4.558$	Upper limit

where,

$f(BU) = (BU/BU_0 - a)$, $f(BU) \geq 0$ (Burnup Correction)
$f(P,pc) = \exp[-(P - 0.04)] \cdot \exp[-(pc/pc_o) \cdot b]$, $(P - 0.04) \geq 0$ (Porosity & Pressure Correction)

$\Delta V/V$ = volume swelling
T(˚C) = temperature
BU (MWd/kg) = burnup
P (/) = porosity
pc (MPa) = contact pressure
a,b (/) = model parameters
BU_0 = 10 MWd/kg = constant
pc_o =constant

Model parameter 'a' can be used to delay the onset of gas bubble swelling, varying between 0 and 5% burnup. Model parameter 'b' influences the effects of contact pressure, and it can be used to emphasize or suppress its effects; it varies from 0 to 1 [15].

2.3.2 DENSIFICATION

Additionally, one must consider that the pore-void volume present in the fuel will be transported to the fuel-cladding gap through densification; this is especially important in a fuel like UC where increased porosity is being considered as a method to compensate for swelling. Of particular interest is whether densification in carbide fuel pins could guarantee a continuous reduction of the cladding strain rate up to a medium burnup.

Dienst analyzed irradiated fuel pins and determined that (U,Pu)C of high porosity will increase in density to about 90% TD by irradiation induced densification, and that a rate constant of 1/1.5 (at% burnup)$^{-1}$ is a conservative choice for process. Additional tests

were performed on 85% theoretical density ($U_{0.85}Pu_{0.15}$)C pellets; the resultant equation is indicative of the decrease in porosity (and volume):

$$\Delta P = \Delta P_{total} [1- \exp(-B/B_{densif})]$$

where ΔP_{total} = -3.4 vol%, B = burnup, and B_{densif} = 0.6at% U+Pu.

Based on the work of Dienst, it is evident that densification of the fuel will occur almost immediately with the onset or irradiation. In other words, before significant PCMI can occur, densification has already completed, and essentially acts as an initial gap increase [22].

2.3.3 Fission Gas Release

In general, the most important motivation in understanding FGR stems from the behavior of the inert gases Xe and Kr; their presence not only degrades the thermal conductivity of the gap, but also causes an unwelcomed pressure increase.

The fundamental factors to consider with regards to the fission gas release (FGR) rate are temperature, burnup, porosity, and grain size. Additionally, stoichiometry, pore-size distribution, cracking, and manufacturing method play an integral role in the rate of release from the fuel [15].

However, most irradiation experiments to date have focused on the swelling properties of carbides. Consequently, data on carbide fission gas release is limited; a lot of what is known stems from (U,Pu)C data. Therefore, a detailed fission gas model that is dependent on each of the factors above is not available. For now, only generalities about the gas release behavior of carbides can be made; most studies focus on the effects of temperature, burnup, porosity, and the breakaway effect.

Lambert noted that up to 60% of the fission gas generated within carbide fuel is retained within the matrix [13]. In large, this behavior can be attributed to the relatively flat temperature profile of carbides; fission gases are trapped within the defects of the carbide matrix. As to be expected, a high-density fuel tends to retain more fission gas than that of a lower density fuel. Nonstoichiometric fuels, which contain more voids than stoichiometric fuels, have the ability to store more fission gas.

Preusser analyzed the available experimental data of both UC and (U,Pu)C and proposed a very simplistic model based only on temperature and burnup. For temperature dependence, three separate regions were describes for the fission gas release rate. Below a central fuel temperature of 1000˚C, very little fission gas release occurs and is taken to be zero. For the region above 1000˚C and below 2070˚C, a linear increase in the fission gas release rate is assumed. Beyond 2070˚C very little data exists, however the available data does show a high release rate, perhaps because the temperature is approaching the melting point [15].

$$\begin{aligned} f^{gas} &= 0 && \text{T} < 1000^{\circ}\text{C} \\ f^{gas} &= 0.000467\text{T} - 0.467 && 1000^{\circ}\text{C} \le \text{T} < 2070^{\circ}\text{C} \\ f^{gas} &= 0.741918*\ln(0.7675\text{T}) - 4.968477 && \text{T} \ge 2070^{\circ}\text{C} \end{aligned}$$

Additionally, a relationship was developed which describes the onset of fission gas release as it relates to percent burnup. BU^{free} is the percent burnup at which FGR begins. It is dependent on temperature.

$$\begin{aligned} BU^{free} &= 2 && \text{T} < 1455^{\circ}\text{C} \\ BU^{free} &= -0.0023\text{T} + 5.3504 && 1455^{\circ}\text{C} \le \text{T} < 2325^{\circ}\text{C} \\ BU^{free} &= 0 && \text{T} \ge 2325^{\circ}\text{C} \end{aligned}$$

The resulting fission gas release rate is based on both temperature and burnup, and it is determined using the relationship below:

$$FGR = f^{gas}(T) * \{1 - \exp[-1.5(BU - BU^{free})\}$$

CHAPTER III

HEAT TRANSFER IN GAS-COOLED REACTORS

Helium has long been considered for reactor applications. It is particularly well suited as a reactor coolant because it is inert, both chemically and with respect to nuclear reactions. As such, it highly compatible with a wide variety of materials; moreover, the fact that helium isn't corrosive results in extended operating lifetimes of reactor components. Thermodynamically, its suitability for very high temperature applications offers improved operating efficiency.

The primary focus of this chapter is heat transfer in helium-cooled reactors. A brief introduction to gas cooled reactors will be performed followed by a review of the thermophysical properties. Lastly, the principal mechanisms of heat transfer will be presented.

3.1 INTRODUCTION TO & EVOLUTION OF THE GAS-COOLED REACTOR

One of the earliest gas-cooled reactors was the Magnox; the design, which was developed by France and the United Kingdom, featured CO_2 cooling, graphite moderation, metallic natural uranium fuel, and magnesium-aluminum cladding. As a result of using unenriched fuel, it operated with a low power density (~0.1 to 0.5 MWe/m^3). Furthermore, the reactor design had to maintain a relatively low specific power (4 to 5 MWt/tonne) due to the limitations of the fuel and cladding; melting of the clad occurred at 645˚C, and a phase change in metallic uranium occurred at 665˚C.

Oxidation of steel in high-temperature CO_2 was also observed, so coolant temperatures were limited to 360˚C.

Although the general experience with the Magnox reactor was considered satisfactory, the design certainly could have been improved. In particular, increased thermodynamic efficiency and better fuel utilization were necessary. One such design that attempted to improve on these limitations was the advanced gas-cooled reactor (AGR), which was also produced in the United Kingdom; this design utilized an enriched uranium oxide fuel, which allowed for higher fuel temperatures and longer irradiation. The increased burnup was made possible by UO_2's ability to accommodate fission products. Additionally, stainless steel was introduced as the cladding material, which allowed for hotter coolant temperatures and a greater heat flux.

Alternatively, in the United States, another approach was being explored; the high-temperature gas reactor (HTGR) replaced CO_2 coolant with helium in an all-ceramic semi-homogenous core composed of thorium and uranium carbide. Higher operating temperatures were tolerable due to the lack of metal in the core. In turn, the higher operating temperatures translated into improved thermodynamic efficiency. Additionally, the use of a graphite moderator, ceramic core, and helium coolant increased the inherent safety of the system [23].

Table 3.1 Evolution of gas-cooled reactors [23]

Reactor Type	Magnox		AGR	HTGR	GCFR
Date of operation	1965	1972	1976	1976	Design
Moderator	Graphite		Graphite	Graphite	None
Coolant	CO_2		CO_2	Helium	Helium
Fuel	Natural uranium (metallic)		Enriched UO_2 (1.5 to 2.5%)	Highly enriched ^{235}U + Th (coated particles)	Mixed UO_2-PuO_2
Fuel element	Slugs		Rod bundles	Prismatic block or sphere	Rod bundles
Fuel cladding	Magnox		Stainless steel	Graphite or ceramic	Stainless steel
Refueling	Off-load	On-load	On-load	Off-load	Off-load
Pressure vessel	Steel	PCRV	PCRV	PCRV	PCRV
Coolant T_{exit} (°C)	335 to 415		635 to 675	725 to 950	530
Coolant pressure (MPa)	1 to 4		2 to 4	1 to 5	~10
Net steam cycle efficiency	20 to 30%		~40%	~39%	~37%
Core power density [MW(e)/m^3]	0.1 to 0.5		~1.0	2.7 to 3.4	~100
Fuel rating [kW(e)/kg·fissile]	100 to 250		200	~500	~350
Average burnup (MWd/kg)	3 to 4		~20	100	70
Conversion ratio	~0.8		~0.6	0.65 to 0.9	1.4 to 1.5
30-yr ore requirement [tonnes U_3O_8/MW(e)]	10		5	2.7	Depleted uranium

In order to calculate the heat transfer and temperature across the core, a detailed review of helium's thermophysical properties is necessary. Only the essential properties for steady-state behavior modeling are considered.

In 1970, the Danish Atomic Energy Commission released a report of the relevant thermophysical properties for helium-cooled reactor technology. A survey of the available experimental data and theoretical data was performed, and a best-fit estimation of the relevant properties was derived. The determined relationships are considered valid from room temperature to 1800K and at a pressure of 1 to 100 bar [24]. Their findings were as follows:

Table 3.2 Thermophysical properties of helium [23]

Gas Law of Helium

$Z = 1 + 0.4446\ (P/T^{1.2})$

P = pressure (bar)
T = temperature (kelvin)
Z = compressibility factor

The standard deviation is shown to be 0.03% at a pressure of 1 bar and 0.3% at a pressure of 100 bar, as determined by the equation $s=0.03P^{1/2}$ [where s is in percent].

Mass Density

$\rho = 48.14\ (P/T)\ [1 + 0.4446\ (P/T^{1.2})]^{-1}$

ρ = density (kg/m^3)
P = pressure (bar)
T = temperature (kelvin)

Again, the standard deviation is shown to be 0.03% at a pressure of 1 bar and 0.3% at a pressure of 100 bar, as shown with the gas law standard deviation.

Specific Heat

$c_p = 5195$ J/kg-K
$c_v = 3117$ J/kg-K

At 273K and a pressure of 1 bar, the standard deviation is 0.05%, and at 273K and 100 bar the standard deviation increases to 0.5%, as determined by $\sigma=0.05P[0.6 – 0.1(T/To)]$ [where σ is in percent].

Coefficient of Dynamic Viscosity

$\mu = 3.674 \times 10^{-7} T^{0.7}$

μ = coefficient (kg/m-s)
T = temperature (kelvin)

The standard deviation is shown by the relationship s=0.0015T [where s is in percent]. At 273K, a deviation of 0.4% is reported, and at 1800K a deviation of 2.7% is determined.

Coefficient of Thermal Conductivity

$k = 2.682 \times 10^{-3}\ (1 + 1.123 \times 10^{-3} P)\ T^{[0.71\ (1-2E-4\ P)]}$

k = thermal conductivity (W/m-K)
P = pressure (bar)
T = temperature (kelvin)

At 273K, the standard deviation is 1.0%, and at 1800K the deviation increases to 6%, as determined by s=0.0035T [where s is in percent].

Prandtl Number

$Pr = c_p\ (\mu/k)$
$Pr = [0.7117 / (1 + 1.123 \times 10^{-3} P)]\ T^{-(0.01 – 1.42E-4P)}$

Pr = Prandtl number
T = temperature (kelvin)
P = pressure (bar)

Where the pressure is in bar, and the temperature is in Kelvin. The standard deviation is determined by the equation s=0.004T [where s is in percent]. At 273K this equates to a 1% deviation and a 7% deviation at 1800K.

3.2 Heat Transfer In a Gas Reactor

A thorough understanding of heat transfer is absolutely essential in determining the temperature profile of a reactor core, i.e. the performance limitations. And given that FRAPCON-3 is only currently capable of modeling water coolant, a review of the heat transfer fundamentals as they apply to helium gas is necessary

Heat generation within the core will be limited to nuclear conditions at steady state. Analysis can be narrowed to the hottest channel within the core because structural and fuel components are the limiting factor in determining reactor power. Additionally, helium can be considered a calorically perfect gas; the specific heat capacity at constant pressure is independent of temperature and pressure [23].

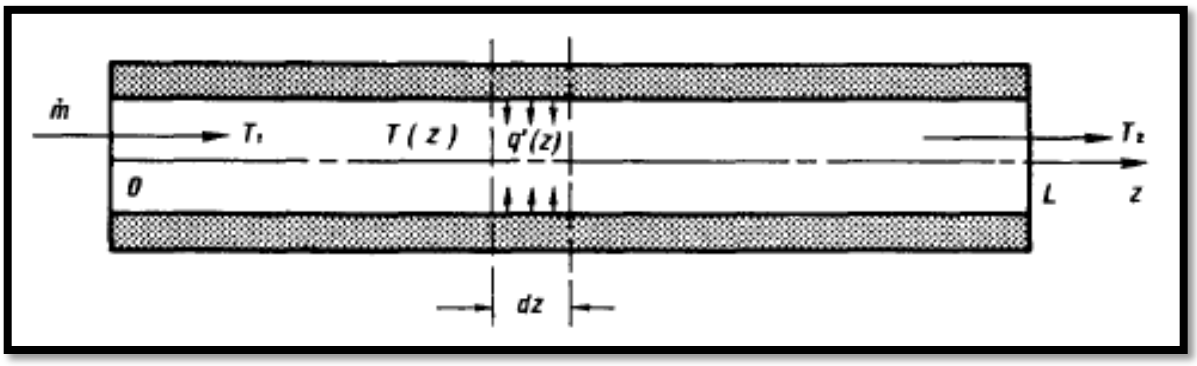

Figure 3.1 Hot channel model [23]

The coolant temperature distribution can be derived by considering a heat balance of the channel:

$$T(z) = T_I + \frac{q}{\dot{m}C_p L}\int_0^z \phi(z)dz$$

T_I – inlet temperature
C_p – specific heat capacity
m – coolant mass flow rate
q – total power produced
L – core length
Φ – axial power variation

After determining the temperature profile of the coolant across the channel, the temperature at the surface must be calculated. Assuming convective heat transfer is the means of transference, Newton's equation can be used:

$q'' = h(T_s - T)$	q" – surface heat flux T_s – surface temperature T – fluid temperature h – heat transfer coefficient

In the core, heat transfer can occur by means of convection, radiation and conduction. However, radiation and conduction have been shown to be negligible during power operation. For steady-state conditions, heat transfer modeling can be greatly simplified by assuming only convective heat transfer. Additionally, negating these modes of transfer results in a more conservative estimate. However, in the event of an accident, this no longer holds true; radiation and conduction are much more pronounced and should be considered.

For turbulent flow, the heat transfer coefficient, h, can be determined by a correlation with the Stanton number or the Nusselt number. They are related by the following:

$St = h/[(m/A)*C_p]$	St – Stanton number h – heat transfer coefficient m – coolant mass flux A – cross-sectional flow area
$St = Nu*Re*Pr$	Nu – Nusselt number Re – Reynolds number Pr – Prandtl number

Alternatively, the Nusselt number alone can be determined. The Dittus-Boelter equation can be used in scenarios with fully developed flow in round holes. The Prandtl

number for all gases ranges from 0.66 to 0.73 and is typically about 2/3 for helium. The Danish Atomic Energy Commission report would indicate the same. Assuming an average of 0.66 for the Prandtl number, the Dittus-Boelter equation for helium could be estimated by: $Nu = 0.0190Re^{0.8}$. Additionally, the Dittus-Boelter is applicable to noncircular ducts if the characteristic length in the Reynolds number and Nusselt number is defined by the hydraulic diameter:

$Nu = 0.023Re^{0.8}Pr^{0.4}$ *[10,000 < Re < 100,000]*	Nu – Nusselt number Re – Reynolds number Pr – Prandtl number
$D_e = 4A/P_f$	D_e – hydraulic diameter A – flow area P_f – wetted perimeter

Although the Dittus-Boelter correlation yields a reasonable estimate, it has been suggested that a correction factor is necessary in conditions where a large temperature gradient exists between the surface and the fluid; helium-cooled reactors are especially likely to experience large temperature changes. Based on an extensive review of experimental data, a correlation for large temperature gradients was developed by McEligot:

$Nu = 0.021\ Re^{0.8}\ Pr^{0.4}\ (T_s/T)^{-0.5}\ [1 + (z/D)^{-0.7}]$ *[15,000 < Re < 600,000]* *z/D > 5* *1 < (Ts/T) < 2.4*	Nu – Nusselt number Re – Reynolds number Pr – Prandtl number T_s/T – Surface-to-Fluid Temp (K) z/D – channel length-to-diameter

Experimental data has shown that the Dittus-Boelter equation based on the equivalent hydraulic diameter varies with the spacing between rods and the rod diameter. Most reactors use a fuel element composed of an array of rods, and a large degree of

experimental data has been used to correlate the Nusselt number the spacing of the bundle. The packing factor, G, is defined by:

$$G = 1 + 0.912Re^{-0.1}Pr^{0.4}[1 - 2.0043\exp(-B)] \quad \text{where, } B = D_e/d$$

As an example, consider the figure below. The packing factor variation as it relates to the pitch-to-diameter ratio is plotted for the case of a triangular array with $Re = 10^5$ and $Pr = 0.67$. In general, tightly packed bundles have the effect of reducing the Nusselt number, where as open arrays of rods are corrected by a number greater than 1.

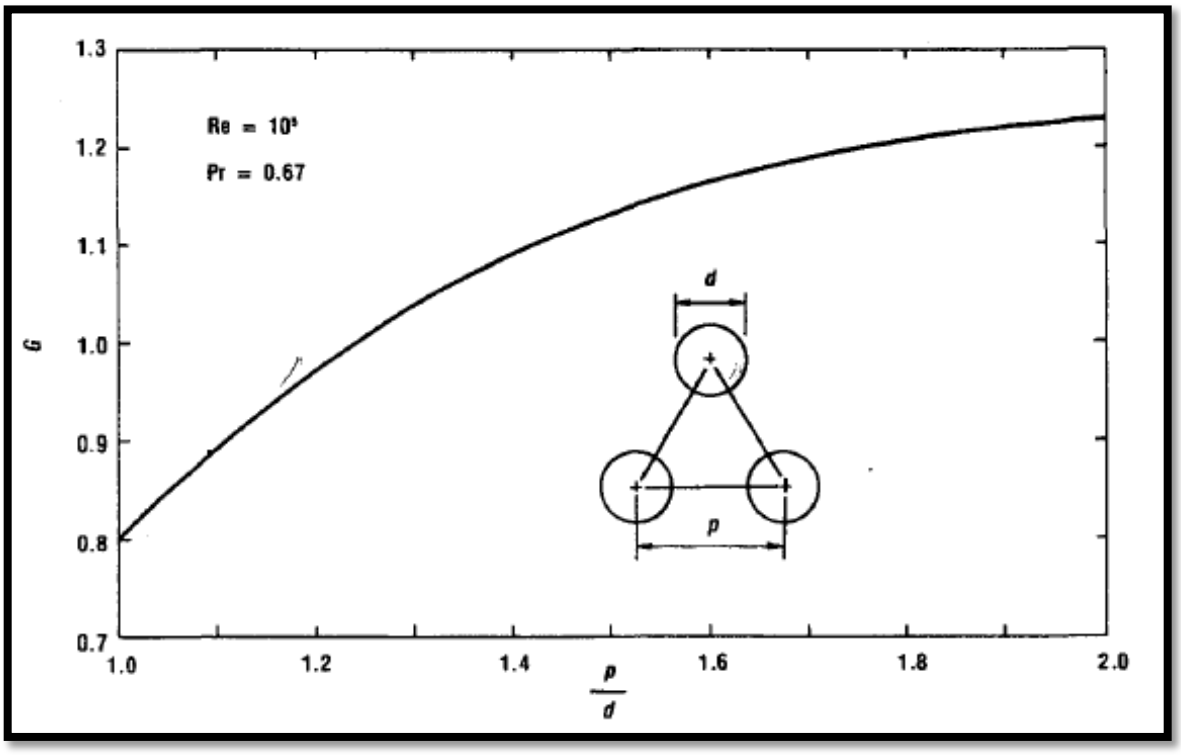

Figure 3.2 Effects of packing factor on Nusselt number [23]

CHAPTER IV

AN INTRODUCTION TO FRAPCON-3.4

FRAPCON-3.4a is an analytical computer code developed by Pacific Northwest National Laboratory (PNNL) under the sponsorship of the U.S. Nuclear Regulatory Commission (NRC). The primary purpose of the code is to calculate the steady-state performance of a light-water reactor fuel rod under long-term burnup conditions. The temperature, pressure, and fuel rod deformation are all calculated as functions of time-dependent fuel rod power and coolant boundary conditions. Currently, the modeled phenomena include:

1. Heat conduction through the fuel and cladding to the coolant
2. Elastic and plastic deformation of the cladding
3. Axial and hoop strain of cladding
4. Mechanical interaction of fuel and cladding
5. Fission gas release from the fuel & rod internal pressure
6. Cladding oxidation & hydriding
7. Fuel densification & irradiation swelling

In practice, the NRC uses it as a tool in their evaluation of fuel performance codes and fuel design changes that are submitted for licensing by fuel vendors [13].

4.1 LIMITATIONS OF CODE

FRAPCON-3.4a is limited to modeling UO_2 pellets in zirconium alloy cladding with a gas gap under light and heavy water reactor conditions. In other words, alternative fuel designs and coolants are not supported (such as metallic fuels or liquid sodium coolant); changes to the current model would be necessary in order to accommodate such

designs. In short, the user can only select specific combinations of reactor, cladding, and fuel types. Table 4.1 outlines these conditions.

Table 4.1 FRAPCON-3.4a Capabilities

Reactor Type	Fuel Type	Cladding Type
BWR	UO_2	Zirc 2
PWR	MOX	Zirc 4
CANDU	Urania gadolinia	M5
	UO_2 w/ ZrB_2 coating	Zirlo

Additionally, the code has only been validated up to a rod average burnup of 62 GWd/MTU; however, the code should render reasonable predictions beyond this. Furthermore, FRAPCON has not been validated beyond the melting temperature of the fuel and cladding, at which point the code stops.

The currently implemented thermal and gas release models are not capable of analyzing rapid power changes because they are based on steady-state conditions and slow power ramp data. As such, the user-input time steps should be no greater than 50 days [26,27,31].

4.2 Code Structure & Solution Scheme

FRAPCON employs an iterative approach when calculating the interrelated effects of fuel and cladding temperature, fuel and cladding deformation, and the fission product generation and release, void volume, and fuel rod internal gas pressure.

The flowchart presented in Figure 4.2 is a simplified representation of the solution scheme. Firstly, the user-input data is processed before the initial fuel rod state is determined through a self-initialization calculation. At each user-specified time-step, a steady-state solution is performed, and a new fuel rod state is determined. The resultant

fuel rod state provides the initial state conditions for the next time step. The code continues to cycle in this manner for the user-specified number of steps.

In simplest terms, the solution for each time step consists of calculating 1) the fuel and cladding temperature; 2) the fuel and cladding deformation; and 3) the fission gas production and release, void volume, and fuel rod internal gas pressure. The fuel rod response for each time step is determined by repeated cycling through two nested loops of iterative calculations until the fuel-cladding gap temperature difference and internal gas pressure converge, i.e. less than a 1% change.

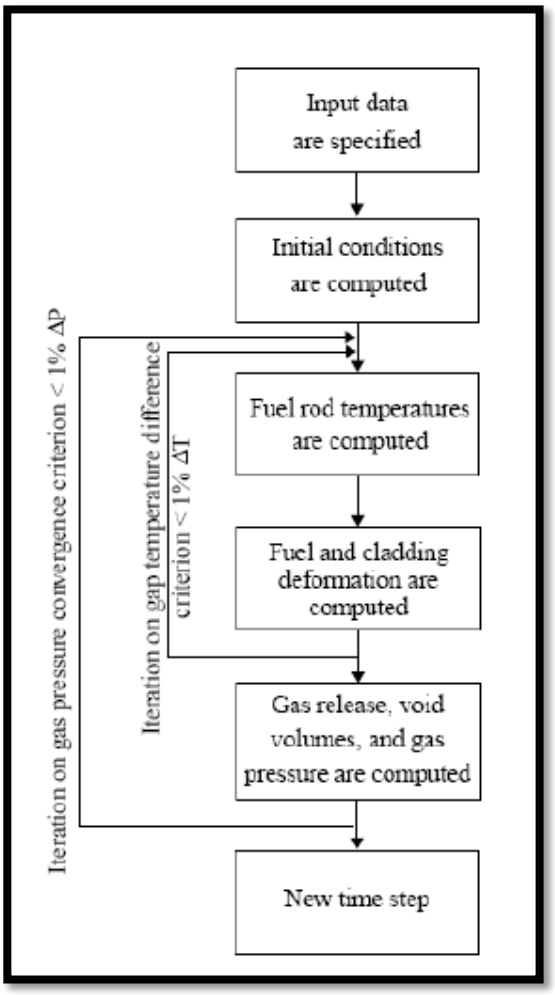

Figure 4.1 Simplified solution flowchart [26]

The inner loop of the solution scheme iterates on the gap temperature. Firstly, the gap conductance is computed using the fuel-cladding gap from the previous time step. From this, a temperature distribution across the rod can be computed. The temperature profile drives the deformation calculation by influencing the thermal expansion of fuel and cladding, as well as the cladding stress-strain relation. From this, a resultant gap distance is calculated, and a new temperature profile can be determined. This alternating process of determining temperature and deformation is repeated until two successive cycles have less than a 1% change in gap temperature.

The outer loop of the solution scheme iterates on the gas pressure within the gap. Each calculation of the loop alternates between the fuel rod temperature-deformation calculation (inner loop) and the fuel rod void-volume gas pressure. For each cycle through the outer loop, the moles of gas are calculated and a pressure is calculated; this is in turn sent back to the deformation and temperature calculation. This alternating process continues until two successive cycles have less than a 1% change in gas pressure [26,27,31].

4.3 Thermal Model

At each axial node, a temperature profile for the coolant and fuel rod is calculated. The currently implemented models assume that the fuel rod is a right circular cylinder surrounded by coolant. Heat conduction is only considered in the radial direction because of the large length-to-diameter ratio, i.e. axial heat conduction is ignored. Additionally, the fuel rod is considered axisymmetric, and heat conduction in the azimuthal direction is ignored. Lastly, steady-state heat flow is assumed.

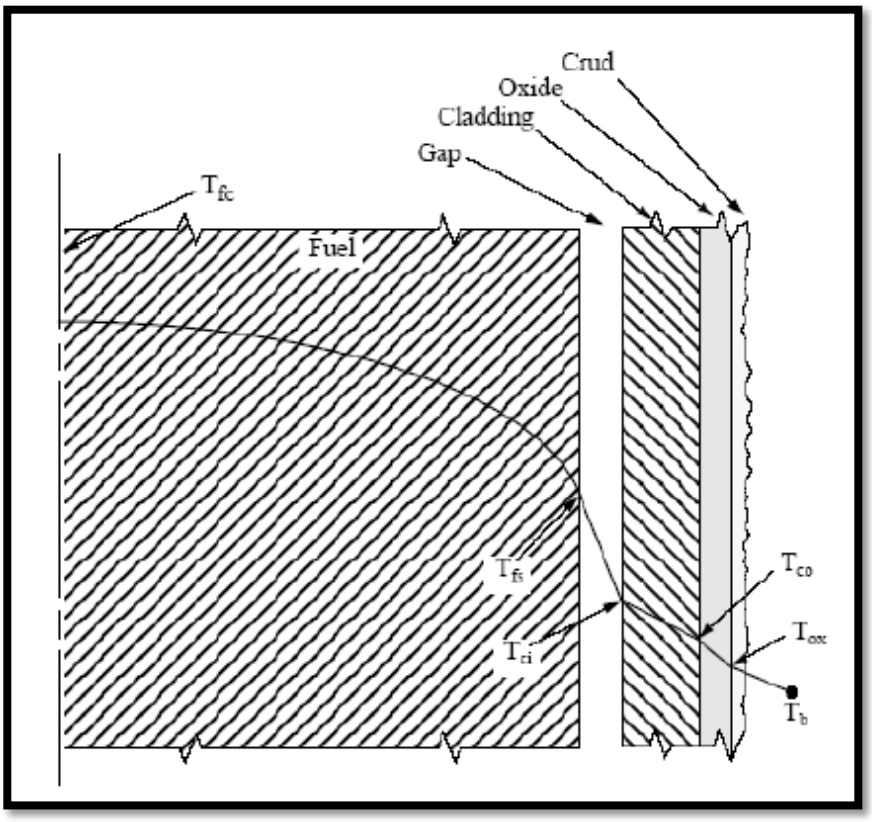

Figure 4.2 Temperature profile of fuel rod [26]

The bulk coolant temperature, T_b, is calculated using a single, closed coolant channel enthalpy rise model:

$$T_b(z) = T_{in} + \int_0^z \left[\frac{(\pi D_0)\, q''(z)}{C_p G A_f} \right] dz$$

$T_b(z)$ = bulk coolant temperature at elevation z on the rod axis (K)
T_{in} = inlet coolant temperature (K)
q"(z) = rod surface heat flux at elevation z on the rod axis (W/m^2)
Cp = heat capacity of the coolant (J/kg-K)
G = coolant mass flux ($kg/s\text{-}m^2$)
Af = coolant channel flow area (m^2)
D_o = outside cladding diameter (m)

And with the exception of heat capacity, all of the parameters above are user-defined.

Next, the cladding surface temperature, T_{co}, is calculated. Two possible methods of heat transfer are considered: forced convection and nucleate boiling. The temperature is taken as a minimum value of the following:

$$T_{co} = T_b + \Delta T_f + \Delta T_{cr} + \Delta T_{ox}$$

$$T_{co} = T_{sat} + \Delta T_{JL} + \Delta T_{ox}$$

$T_b(z)$ = bulk coolant temperature (K)
$T_w(z)$ = rod surface temperature (K)
$\Delta T_f(z)$ = forced convection film temperature drop K)
$\Delta T_{cr}(z)$ = crud temperature drop (K)
$\Delta T_{ox}(z)$ = oxide layer temperature drop (K)
T_{sat} = coolant saturation temperature (K)
ΔT_{JL} = nucleate boiling temperature drop (K) Jens-Lottes correlation

At each time step, the rod temperature (as calculated by each heat transfer method) is determined, and the minimum value is chosen; in this way, the code establishes whether forced convection or nucleate boiling is occurring. For forced-convection, the coolant film layer at the rod surface is based on the Dittus-Boelter film conductance, and for nucleate boiling heat transfer, the temperature drop across the coolant film layer is based on the Jens-Lottes formulation.

The inner clad surface temperature, T_{ci}, is found by calculating the temperature rise across zirconium oxide and the cladding using Fourier's law. Again, it is assumed that steady-state heat transfer is occurring, and that the fuel rod is a cylinder of uniform thermal conductivity:

$$\Delta T_c = q''(z) r_o \ln(r_o / r_i) / k_c$$

ΔT_c = cladding temperature drop (K)
r_o = cladding outside radius (m)
r_i = cladding inside radius (m)
k_c = temperature and material dependent thermal conductivity of the cladding (W/m-K)

The temperature rise to the fuel surface is determined from an annular gap conductance model, thereby establishing the fuel surface temperature, T_{fs}. Gap conductance, h_{gap}, is responsible for the temperature drop between the fuel surface and the inner cladding. In other words, it is the sum of three conduction routes: 1) Conduction through the gas gap; 2) Conduction through areas of contact; 3) Radiative heat transfer:

$$\mathbf{h_{gap} = h_{gas} + h_{contact} + h_{rad}}$$

Lastly, the temperature distribution in the fuel is calculated, accounting for fuel cracking effects using fuel surface temps and assumed symmetry at the centerline boundary conditions. Additionally, the temperature profile is based on the fuel type, reactor type and burnup. The fuel-pellet heat conduction model employed by FRAPCON is based on a finite difference approach.

Once a fuel temperature distribution has been determined, FRAPCON estimates a gap temperature drop. Should the gap temperature drop converge on a value, the iterative solution will stop, and the mechanical model will begin. However, if the gap temperature drop does not converge on a value, a new conductance will be determined and a resultant fuel temperature distribution will be calculated. This process will be repeated until a solution converges on a gap temperature difference < 1%. An outline of the thermal model can be seen in Figure 4.4 [26,27,31].

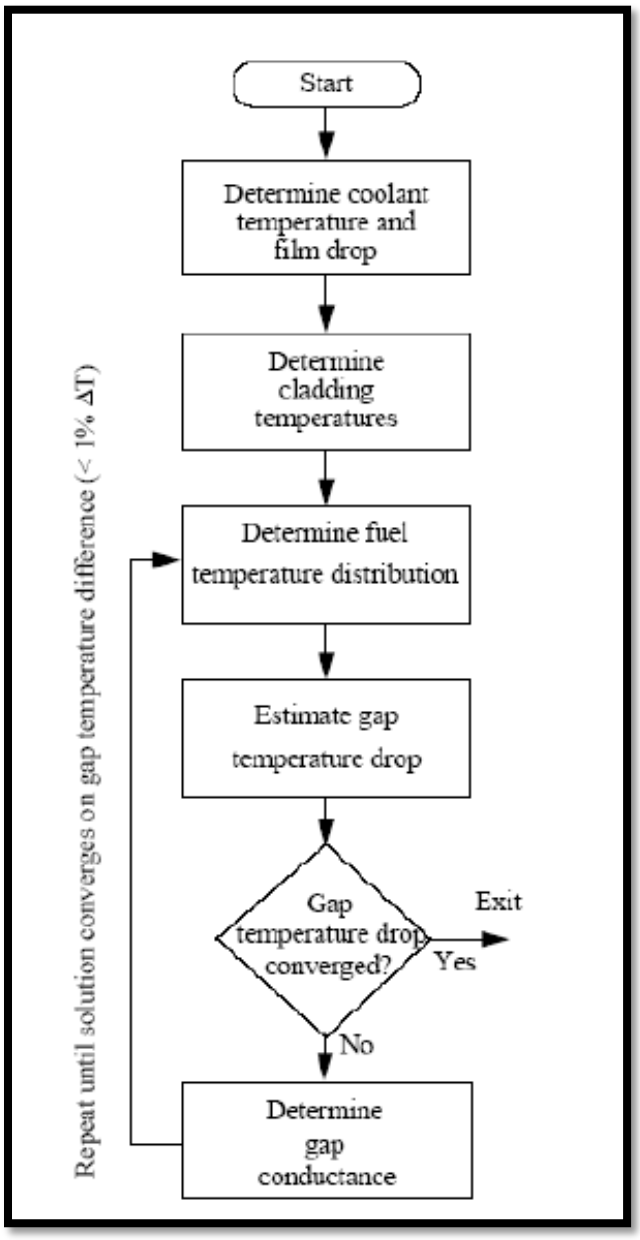

Figure 4.3 Flow chart of the fuel rod distribution profile calculation [26]

4.4 MECHANICAL MODEL – FRACAS-I

As shown in Figure 4.2, there is a close coupling of the thermal and mechanical models due to the fuel-cladding gap. Once a thermal profile for the fuel rod has been determined, FRACAS-I (the default mechanical model) begins iterating. FRAPCON assumes the fuel pellet to be rigid and ignores any stress-induced deformation.

In the analysis for fuel deformation, two situations are considered: an open-gap regime and a closed-gap regime. In an open-gap regime, the fuel and cladding have yet to come into contact, and the problem of a cladding with internal and external pressures and a temperature distribution must be solved. In a closed-gap regime, the fuel has expanded to the point at which the fuel comes into contact with the cladding. Thermal expansion, swelling of the fuel, relocation, and cladding creep can all contribute to the 'closed-gap' regime.

In FRAPCON-3, deformation analysis is based on analysis that includes stresses, strains, and displacements in the fuel and cladding for the entire rod. Additionally, it is assumed that the cladding retains its shape during deformation. FRACAS-I is made up of a cladding deformation model as well as a fuel deformation model. And should the fuel come into contact with the cladding (closed-gap regime), a driving force will be applied to the cladding deformation model. However, as the model is currently implemented, cladding deformation does not influence fuel deformation in any way.

4.4.1 Cladding Deformation

In FRACAS-I, the cladding deformation model assumes:

1. The incremental theory of plasticity
2. Prandtl-Reuss flow rule
3. Isotropic work-hardening
4. Thin wall cladding (stress, strain, and temperature uniform throughout)
5. No axial slippage at fuel/cladding interface (when in contact)
6. Bending strains & stresses in cladding are negligible
7. Axisymmetric loading & deformation of cladding

4.4.2 Fuel Deformation

In FRACAS-I, the fuel deformation model assumes that thermal expansion, swelling, and densification is the only source of deformation. The pellet is considered to be a perfect cylinder with isotropic properties. Additionally, the fuel experiences no resistance to expansion and does not experience creep deformation. Lastly, the model accounts for the effects of relocation by not allowing hard contact between fuel and cladding until swelling and thermal expansion recover 50% of the relocated pellet radius.

Radial deformation is calculated with a free-ring expansion model:

$$\mathbf{R_H = \Sigma\ \Delta r_i\ [1 + \alpha_{Ti}\,(T_i - T_{ref}) + \varepsilon^S + \varepsilon^d]}$$

R_H = hot-pellet radius (m)
α_{Ti} = coefficient of thermal expansion of the i-th radial temperature (1/K)
T_i = average temperature of i-th radial ring (K)
T_{ref} = reference temperature (K)
Δr_i = width of i-th radial ring (m)
ε^S = swelling strain
ε^d = densification strain

Densification asymptotically approaches the ultimate density change, over a local burnup of 5 GWd/MTU; beyond such burnup, all densification has presumed to taken place and is no longer considered.

Fuel swelling is solely attributed to the athermal swelling associated with solid fission product accumulation; gaseous fission products are currently not considered. Swelling is linear with burnup, and it doesn't onset until a burnup of 6 GWd/MTU is achieved. The delay is to account for swelling into the as-fabricated porosity. After which, swelling accumulates at a rate of 0.062 vol% per GWd/MTU up to 80GWd/MTU; after, the rate increases to 0.086 vol% per GWd/MTU.

In order to better understand fuel deformation as it is calculated in FRAPCON 3.4, a test case has been presented. In Figure 4.5, the results of a PWR operating under a

constant power of 8 kW/ft are presented. The dashed line denotes the total fuel deformation over a period of time. Notice that the graph has been sectioned into 3 regions: open gap, soft contact, and hard contact.

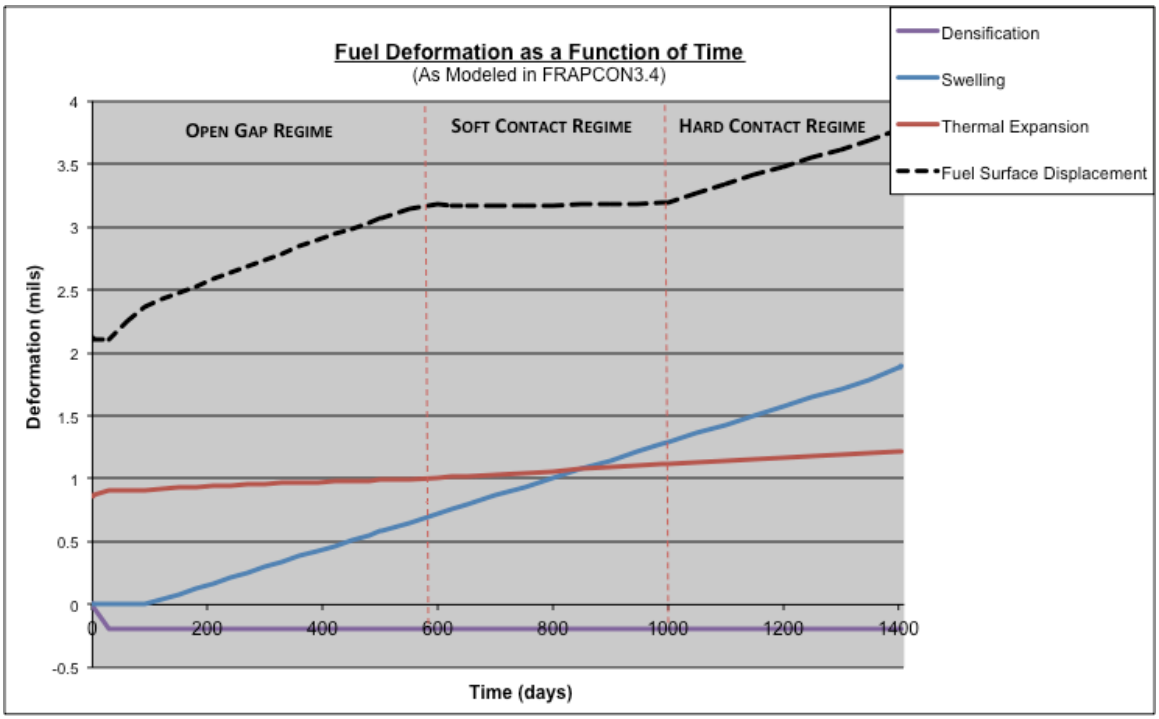

Figure 4.4 Fuel deformations as a function of time

As examined previously, FRACAS-I attributes all fuel deformation to densification, irradiation induced swelling, and thermal expansion; irradiation induced creep or thermal creep has no effect on the pellet. Additionally, the fuel experiences no resistance to swelling, i.e. the cladding has no bearing on fuel deformation. In **Figure 4.5**, fuel displacement is plotted as a function of time. Additionally, the individual components (swelling, expansion, and densification) of deformation are plotted.

The purple line illustrates the densification of the fuel. Notice that a small negative change in the fuel surface is attributed to the process. This occurs very early during irradiation, and it is assumed to have completed by 5 GWd/MTU. Its initial, dominant influence on fuel displacement can be seen in the very beginning of the fuel displacement.

Once densification has completed, deformation of the fuel is entirely a function of swelling and thermal expansion. In the figure above, the blue line represents fuel displacement due to swelling. The onset of swelling is delayed; after which time, deformation due to swelling accumulates linearly with burnup. Notice that at a constant power, swelling is the primary contributor to the increasing fuel deformation.

Lastly, the red line depicts the contribution of thermal expansion to the dimensional change in the pellet. In this case, a constant power was used so the pellet experienced minimal temperature change. Consequently, thermal expansion contributed only a small amount to the fuel deformation over time. Its effects are more pronounced in startups, shutdowns, and power ramps.

When summed, the effects of densification, swelling, and thermal expansion equal that of fuel deformation (dashed black line in **Figure 4.5**). However, notice that no additional deformation accrues during soft contact. Expansion and swelling must recover 50% of the relocated pellet radius before hard contact can occur; during this period no additional fuel deformation can occur.

4.4.3 The Effects of Relocation And Recovery

Rapid temperature changes (such as that experienced during start-up and shutdown) cause the fuel pellet to crack; this is due to the thermal hoop stresses and the

differential thermal expansion generated across the fuel pellet. Cracking promotes an outward relocation of the pellet fragments, effectively altering the as-fabricated gap distance. The shortened distance between the fuel and cladding improves the heat transfer across the fuel rod. Additionally, it reduces the time that is necessary for contact between the fuel and cladding to occur [26, 27].

Currently, FRAPCON-3.4 accounts for the effects of relocation through the use of two separate mechanisms. In the first, a "thermal gap distance" is calculated; this value is included in the thermal and internal pressure calculations only. In the second, a "mechanical gap" distance is determined; this value is used only with respect to mechanical deformation and in order to determine the contact regime, i.e. soft/hard contact.

The thermal gap distance calculation is based on a model developed for the GAPCON-THERMAL-2 Rev.2 (GT2R2) code. Using the linear heat generation rate and the burnup, a multiplication factor is determined and applied to the cold-state gap distance. The resultant value is the effective change in distance due to relocation.

$\Delta G/G = 30 + 10*FBU$	LHGR < 20 kW/m
$\Delta G/G = 28 + PFACTOR + (12 + PFACTOR)*FBU$	20 kW/m < LHGR < 40 kW/m
$\Delta G/G = 32 + 18*FBU$	LHGR > 40 kW/m

where,

$\Delta G/G$ = decrease in hot gap, based on as-fabricated cold gap dimensions (%)

LHGR = linear heat rate (kW/m)

FBU = BURNUP/5, for BURNUP < 5 GWd/MTU
= 1, for BURNUP ≥ 5 GWd/MTU

PFACTOR = (LHGR – 20)*5/20

As shown above, the FRAPCON-3 relocation model predicts anywhere between 30 to 50% change in the as-fabricated gap, a range which was determined through comparison with benchmark cases. And this calculated gap distance is only applicable in subsequent calculations involving the gap pressure and the temperature profile across the rod. Additionally, it is only valid when used with the thermal conductivity of an uncracked pellet; in other words, the relocation constant acts as correction factor for the change in thermal conductivity as well.

Figure 4.6 shows the effect that burnup & linear heat generation rate can have on the as-fabricated gap distance. Increasing burnup reduces the gap size, an effect that saturates at 5 GWd/MTU. Additionally, a higher heat generation rate has the same effect.

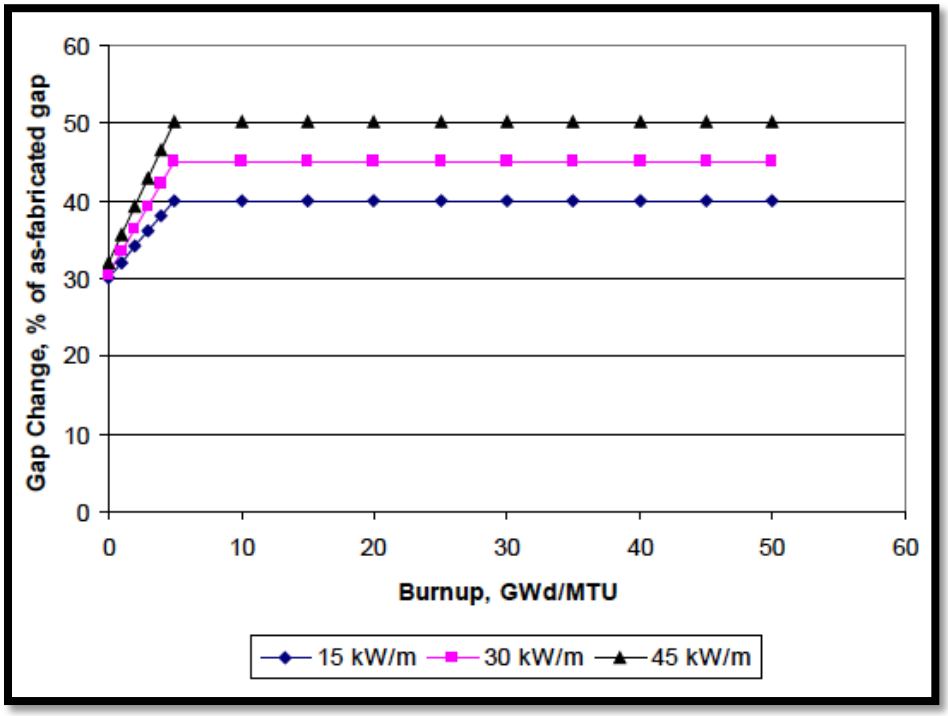

Figure 4.5 Effects of power and burnup in GAPCON relocation model [26]

For comparison, the current relocation model of FRAPTRAN 1.3 (NRC's transient analysis code) was reviewed. Because the GAPCON model is burnup dependent and FRAPTRAN has no significant burnup over the time periods of events, a much simpler model is implemented. For fresh fuel, relocation is assumed to occupy 30% of the initial gap size. And for irradiated fuel, relocation is assumed to be 45% of the gap [26, 27].

Additionally, a mechanical gap calculation is performed; this gap distance is exclusive to FRACAS I, the mechanical deformation model. As noted earlier, two scenarios are possible within FRAPCON: open gap and closed gap. And once fuel-clad contact has been established, the closed gap regime must distinguish between soft and hard contact.

The mechanical gap method is used to establish when fuel-clad contact changes from the soft regime to the hard regime. In FRAPCON-3, hard contact between the fuel and the cladding is not allowed until swelling and thermal expansion recover 50% of the original relocated pellet radius, a value which has also been experimentally determined. In other words, no cladding deformation due to fuel swelling and thermal expansion is allowed before then. Half of the relocation must be consumed by the differential pellet-cladding displacements before PCMI occurs. This assumption is based on beginning-of-life measurements for the onset of cladding axial elongation and from Halden squeeze tests; the experimental data shows that roughly half of the assigned relocation must be utilized before the fuel pellet's behavior returns to that of a solid, i.e. hard contact has occurred [26,27,31].

In Figure 4.6, the previous test case is reviewed; however, the thermal and mechanical gaps are displayed alongside fuel deformation. Again, the graph indicates three separate regimes: open, soft contact, and hard contact. The thermal gap distance, as determined by FRAPCON 3.4, is represented by the purple line. Alternatively, the green line is the mechanical gap as calculated by the code.

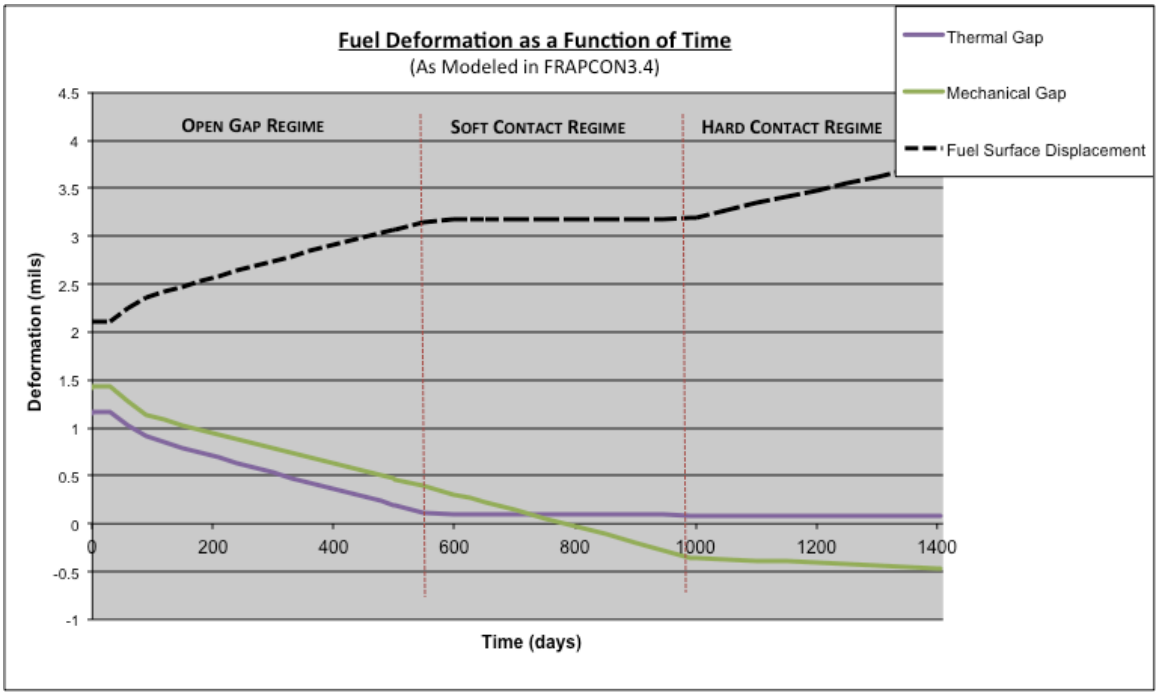

Figure 4.6 Comparison of thermal gap and mechanical gap

First, consider the thermal gap distance; recall that it is based on the GAPCON model and is used in the thermal and internal pressure calculations only. The close of the thermal gap signifies that soft contact has occurred. In Figure 4.6, the thermal gap is closed at the first vertical line; the small remaining gap can be attributed to surface roughness. And it is at this point where no deformation of the fuel can occur until half of

the original relocated pellet radius is recovered. Lastly, the thermal gap can never go below zero.

Alternatively, the mechanical gap continues to close, even after soft contact has occurred. The mechanical gap continues to shrink and becomes a negative value because the initial gap thickness and cladding dimensional changes are less than that of the fuel dimensional changes. This value is used only with respect to mechanical deformation and in order to determine the contact regime, i.e. soft/hard contact. Three factors are considered when calculating the mechanical gap: 1) as-fabricated gap, 2) total fuel deformation, 3) and cladding deformation. Once 50% of the original pellet relocated radius has been recovered, hard contact is assumed. Deformation of the clad due to contact by the fuel is now considered.

CHAPTER V

IMPLEMENTATION INTO FRAPCON

Currently, FRAPCON3.4 has been validated for use with BWRs, PWRs, and HWRs, and the user is confined to the choice of an oxide-based fuel and zirconium-based cladding [26]. Under the guidance of Dr. Travis W. Knight and Dr. Elwyn Roberts, research is being conducted at the University of South Carolina to implement advanced materials and fuel performance models into FRAPCON 3.4, the NRC's preferred steady-state fuel performance code [26]. Collaborative research with Ian Porter and Bo-Shiuan Li expands on these capabilities with the addition of a uranium carbide fuel, silicon carbide cladding, and helium coolant; our efforts are reflected in FRAPCON3.4-USC1.3.

The focus of this chapter is the implementation (coding) and verification of uranium carbide and helium. Additionally, Li's implementation of silicon carbide, as detailed in his thesis work, will be highlighted as well [32]. Our combined efforts will be reflected in a joint research paper.

5.1 IMPLEMENTING URANIUM CARBIDE

The material properties and fission gas model of FRAPCON3.4 have been updated to model the performance of a uranium carbide fuel. Special emphasis has been placed on the thermal performance and the swelling behavior.

As shown in Chapter 2, published literature reflects a high swell rate for uranium carbide. As a means of reducing pellet-clad mechanical interaction, 75 – 90% TD

carbides will be used [21]. Most studies focus on this density range; as such, the implemented physics will reflect a carbide fuel in this range. Additionally, no distinction in composition has been made; at the moment, not enough reliable data exists to draw a conclusive dependence. Furthermore, a literature review reveals that an acceptable correlation with stoichiometry cannot be determined. However, experimental data does show that stoichiometric and slightly hyperstoichiometric fuels perform more advantageously than hypostoichiometric carbides with respect to thermal properties and swelling.

5.1.1 Mechanical Properties

Because FRAPCON assumes a rigid pellet, most mechanical properties relating to the fuel are unnecessary. However, additional properties have been implemented into the program as a means for calculating the cracking behavior impacting on fuel relocation. Table 5.1 highlights the applied mechanical properties for uranium carbide and any assumptions that were made.

Table 5.1 Mechanical properties for UC

Density	
$\rho = 13.63$ g/cm^3	
Poisson's Ratio	
$\upsilon = 0.288 - 0.286P$	P = porosity (/)
Poisson's ratio is valid for a range of 5 to 27% porosity.	
Young's Modulus	
$E = 215(1 - 2.30P)[1 - 0.92E\text{-}4\ (T-25)]$	E = young's mod (GPa) P = porosity (/) T = temperature (˚C)
Young's modulus is valid up to 30% porosity and up to 1250˚C. Stoichiometry and composition are not considered.	

5.1.2 THERMAL PROPERTIES

As discussed previously, FRAPCON 3.4 is a steady-state code. The primary thermal properties of interest are thermal conductivity and thermal expansion. Additionally, the melting temperature is included; however, it is of primary interest only in transient scenarios and in alerting the user to fuel failure. Specific heat is unimportant for these cases, and it is not integrated. Lastly, as discussed previously, FRAPCON assumes a rigid pellet model; consequentially, thermal creep of the fuel is not considered. Table 5.2 highlights the implemented thermal properties for uranium carbide and any assumptions that were made.

Table 5.2 Implemented thermal properties of uranium carbide

Thermal Conductivity

$21.7 - 3.04\times10^{-3}\,T + 3.61\times10^{-6}\,T^2\,[(1-P)/(1+P)]$ ***[50 < T < 700 ˚C]***

$20.2 + 1.48\times10^{-3}T\,[(1-P)/(1+P)]$ ***[700 < T < 2300 ˚C]***

k = conductivity (W/m˚C)
T = temperature (˚C)
P = porosity (/)

The physics above are applicable to stoichiometric and hyperstoichiometric carbides. Composition, burnup, and fission gas content also influence conductivity; however, insufficient data exists to consider their effect [2]. A conservative estimate, as predicted by Lewis & Kerrisk, was implemented [14].

Coefficient of Thermal Expansion

$$\alpha(T) = 1.007 \times 10^{-5} + 1.17 \times 10^{-9}T$$

α = coefficient (1/˚C)
T = temperature (˚C)

The thermal expansion coefficient is entirely dependent on temperature. Composition and stoichiometry are not considered. The Elbel expression was implemented [11].

Melting Temperature

$T_m = 2315$˚C

Melting temperature is applicable to stoichiometric and hyperstoichiometric fuel. The effects of compositions aren't well understood, and are not considered [13].

5.1.3 IRRADIATION INDUCED BEHAVIOR

Irradiation of the fuel gives rise to a number of significant phenomena. Swelling, densification, creep, and fission gas release are among some of the most important. However, as shown before, FRAPCON assumes a rigid pellet and irradiation-induced creep is unaccounted for. Therefore, swelling, densification, and fission gas behavior are the primary phenomena of interest. Table 5.3 highlights all implemented models or properties, as well as any assumptions or simplifications that were made.

Table 5.3 Irradiation behavior of uranium carbide

Swelling

$\Delta V/V = 0.4667 + 1.711 f(P,pc)$ [T < 700˚C]

$\Delta V/V = 0.4667 + 1.711 f(p,pc) + [(6.412 - 0.0198T + 0.152e\text{-}4T^2)\, f(BU)\, f(P,pc)]$ [T > 700˚C]

f(P,pc) = porosity & pressure correction

f(BU) = burnup correction

The proposed swelling mechanism for UC is dependent on burnup, temperature, interfacial pressure, and porosity [15]. This model accounts for total swelling (solid & gaseous products).

Densification

$\Delta P = \Delta P_{total}\,[1\text{-}\exp(-B/B_{densif})]$

P = porosity reduction
P_{total} = -3.4 vol%
B = burnup
B_{densif} = 0.6 at% U+Pu

Diesnt suggested a rapid densification of high porosity mixed carbide fuel up to about 90% theoretical density. Assumed to be completed by

Emissivity

$\varepsilon_t = 0.45$

De Coninck's value for emissivity is applicable to all stoichiometric fuel [16]. It is not temperature dependent.

Fission Gas Release

$$FGR = f^{gas}(T) * \{1 - \exp[-1.5(BU - BU^{free})]\}$$

BU – burnup
BU^{free} – onset of release
f^{gas} – release rate

where,

$f^{gas} = 0$ **[T < 1000˚C]**

$f^{gas} = 0.000467T - 0.467$ **[1000˚C ≤ T < 2070˚C]**

$f^{gas} = 0.741918 * \ln(0.7675T) - 4.968477$ **[T ≥ 2070˚C]**

Based on the experimental data available from Preusser.

5.1.4 Relocation And Recovery

As addressed in Chapter 4, relocation plays an intricate role in determining not only the temperature profile across the fuel, but the mechanical deformation model as well. Given that the FRAPCON-3 relocation model is based on highly empirical data for UO_2, it is not immediately obvious whether it is applicable to carbides, and if so, to what degree. The relevancy is highly dependent on whether the carbide fuel cracks

Calculating the power at which a pellet cracks is integral to evaluating the applicability of the relocation model. By determining the thermal stress that an uncracked pellet experiences during startup and comparing this with the fracture stress, it is possible to estimate the point at which cracking and concomitant relocation will occur. Given a specific linear heat generation rate, the maximum thermal stress can be predicted by:

$$\sigma_{t,\,max} = \frac{\alpha E q'}{8\pi(1-\upsilon)\bar{\lambda}}$$

$\sigma_{t,\,max}$ – maximum thermal stress (MPa)
α – thermal expansion coefficient (1/K)
E – Young's modulus (MPa)
q – linear heat generation rate(W/m)
υ – Poisson's ratio
λ – thermal conductivity (W/m-K)

Because Young's modulus, Poisson's ratio, and thermal conductivity are all a function of porosity, it is necessary to account for the density of the fuel design. For example, consider Table 5.4 and Figure 5.1 below. A comparison is made between the thermal stresses experienced by 100% TD UC, 85% TD UC, and 95% TD UO_2. A simple calculation reveals that carbides can be subjected to a significantly higher linear heat generation rate before cracking; by comparison 85% UC can handle a LHGR ten times that of 95% TD UO_2. Uranium dioxide can crack under the thermal stresses produced by as little as 3 kW/m, and an average LWR operates at 20 kW/m.

Table 5.4 Estimated LHGR needed in order to crack

	95 % TD UO_2	100% TD UC	85% TD UC
Young's Modulus (GPa)	200	200	130
Thermal Conductivity (W/mK)	3.00	20.65	15.25
Poisson's Ratio (/)	0.310	0.288	0.245
Thermal fracture stress (MPa)	130	200	200
LHGR to crack (kW/m)	3.38	32.99	39.75

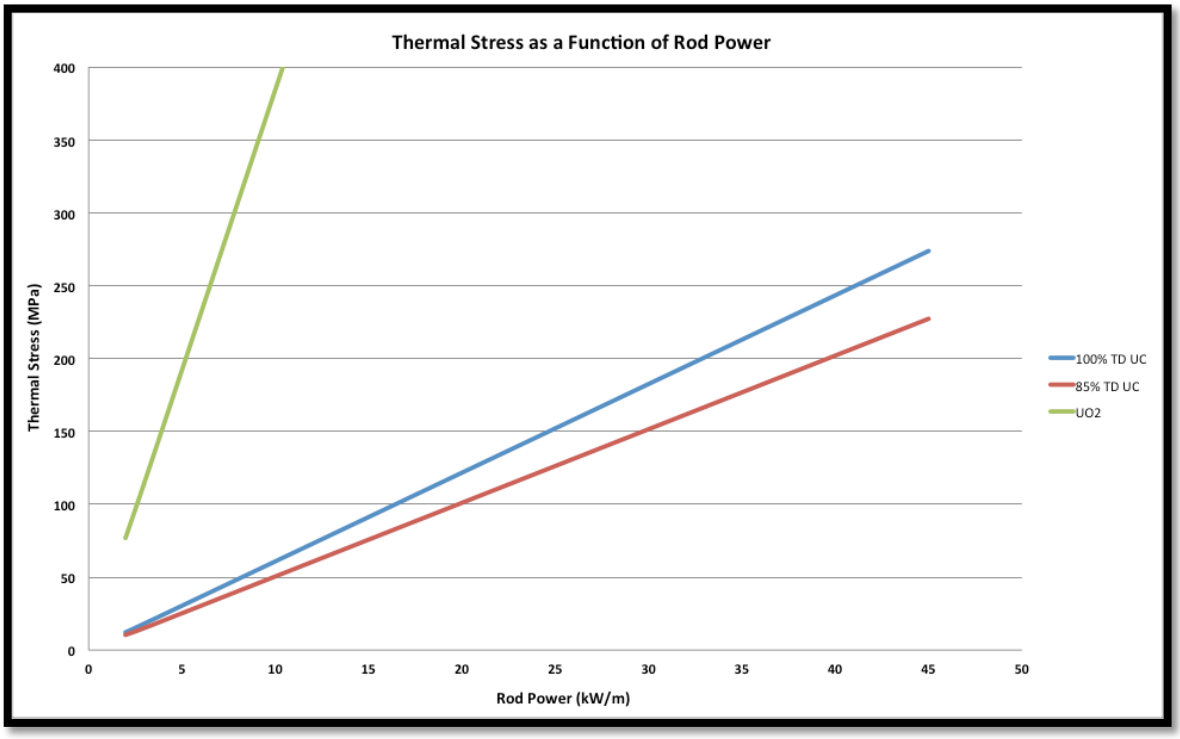

Figure 5.1 Thermal stress vs. power for UO_2 and UC

5.1.5 Implementing A Modified Relocation Model for UC

For carbides, there is no in-pile data available regarding relocation behavior. However, based on the previous calculation, it is evident that cracking will only occur at high linear heat generation rates. Therefore, the GAPCON model that is currently implemented into FRAPCON will be modified. An additional calculation (similar to above) will be performed at the beginning of each time step to determine whether the fuel cracks (or if it cracked in a previous time step). A simplified flow chart seen in Figure 5.2 shows this process.

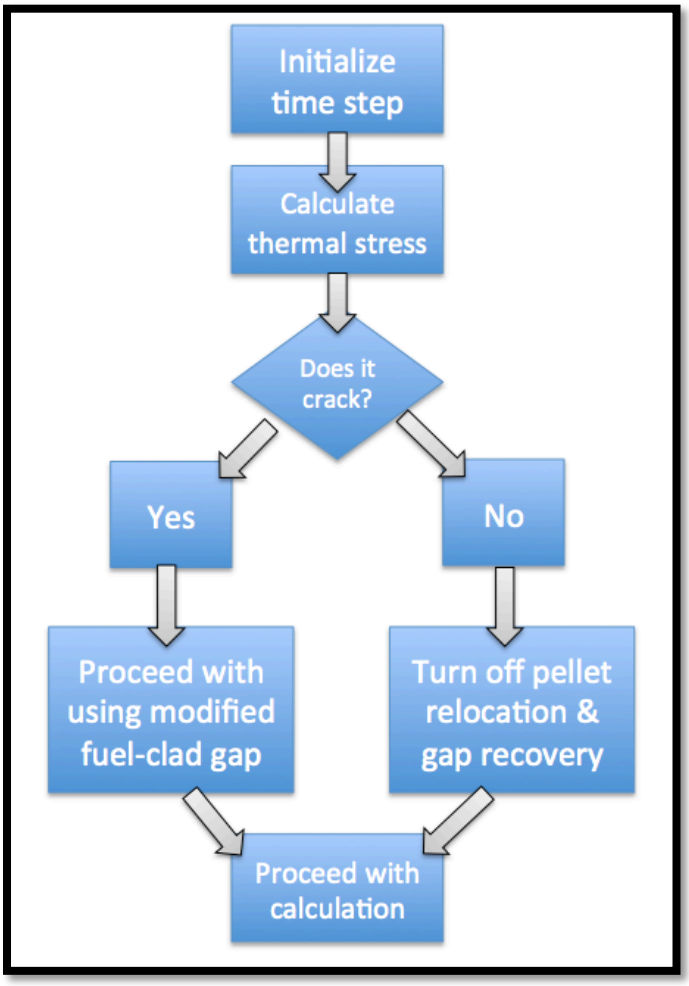

Figure 5.2 Flowchart of modified relocation and recovery scheme

If the fuel does not crack, then the subsequent thermal and pressure calculations will be based entirely on the physical gap distance. As a result we can expect the fuel temperature profile to be higher, due to a larger gap distance and reduced conductance. Furthermore, recovery will be set to zero, i.e. in other words, soft contact will not exists because there will be no void volume created from relocation. Effectively the open gap regime will transition directly into hard contact and bypass the soft contact regime.

Conversely, if the fuel does crack, then it is necessary to account for the effects of relocation and recovery. Currently, there is no data available regarding uranium carbides

relocation behavior. As shown in Chapter 4, the GAPCON model adjusts the hot gap size anywhere between 30 to 50% of the as-fabricated gap distance, and it is based on experimental data. This model is not directly applicable to carbide; however, it is believed that pellet fragments will share fundamental similarities with regards to relocating into the gap. A '*most conservative estimate'* approach will be taken. The gap will be reduced by the smallest amount ~ 30%. This gives the hottest temperature profile. Recall this value is applied to the as-fabricated gap to determine a "thermal gap distance."

Modified Relocation	
ΔG/G = 30	ΔG/G = decrease in hot gap, based on as-fabricated cold gap dimensions (%)

Additionally, the effects of recovery should be considered as they apply to carbides. FRAPCON does not allow hard contact before 50% of the relocation displacement is consumed by the differential pellet-cladding displacement. As shown in Chapter 4, this value has been derived experimentally and is not directly applicable to carbides. It is only appropriate for oxide fuel with a zirconium based clad. Because of the lack of substantial evidence, 50% will be retained as the standard recovery before fuel-clad contact. However, further experimental data will be necessary in order to determine a more appropriate value.

To demonstrate the significance of relocation for uranium carbide, a comparison case was performed in FRAPCON. Identical input conditions were used: PWR conditions, *UC fuel*, water coolant, ZIRLO cladding. In the first case, no relocation occurs, i.e. no cracking. In the second case, the suggested fuel relocation model is turned on, and the fuel is forced to crack; the relocated fragments consume 30% of the as-

fabricated gap distance. Input conditions can be seen in the table below, and in Figures 5.3 - 5.5 the results can be seen. Discussion will follow.

Table 5.5 Input conditions for relocation comparison

Property	Value
Fuel composition	UC
Fuel enrichment (%)	4.5
Fuel theoretical density (%)	85
Fuel pellet type	Solid cylindrical
Fuel pin diameter (mm)	9.144
Fuel pellet diameter (mm)	7.842
Clad thickness (mm)	0.572
Fuel height (m)	3.6576
Coolant pressure (MPa)	15.5
Coolant inlet (K)	564.43
Coolant mass flux (kg/m^{2}s)	15.5
LHGR (kW/m)	18

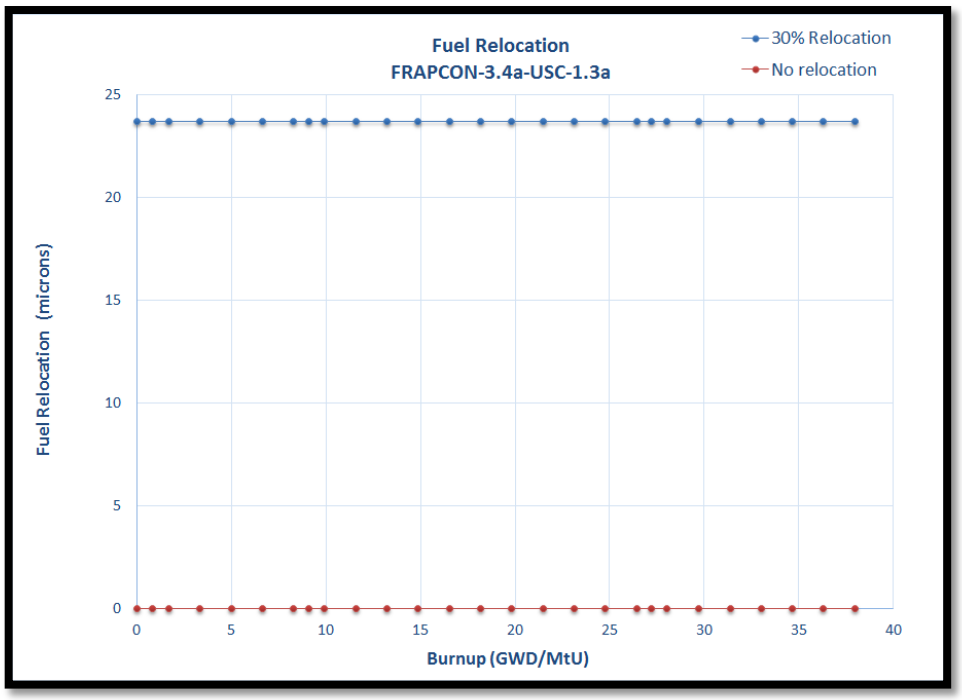

Figure 5.3 Fuel relocation in each test case

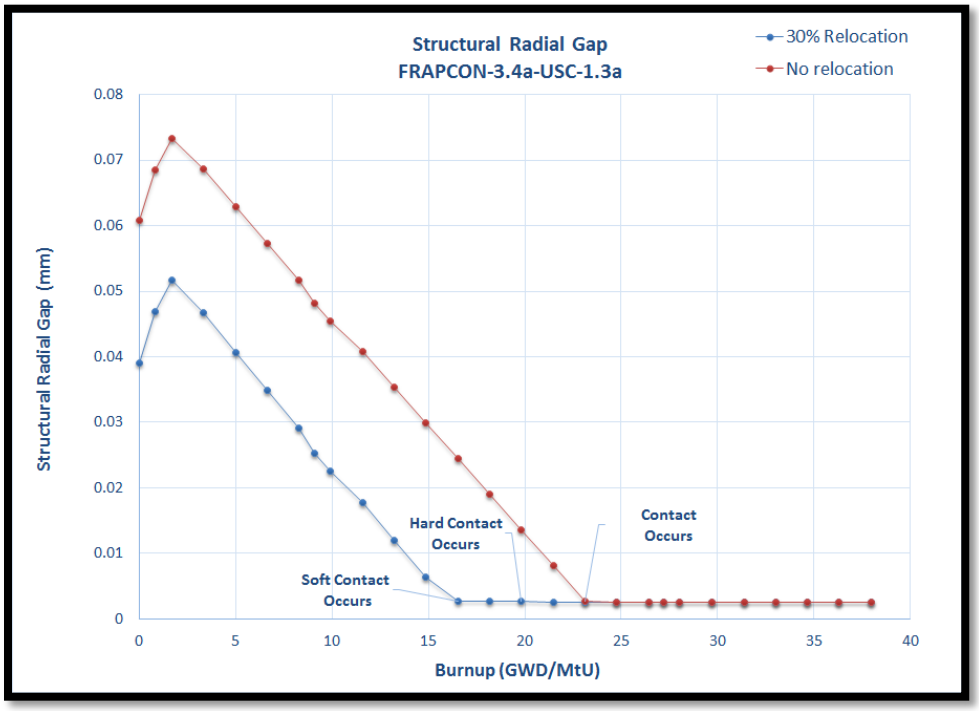

Figure 5.4 Gap closure for relocation and non-relocation

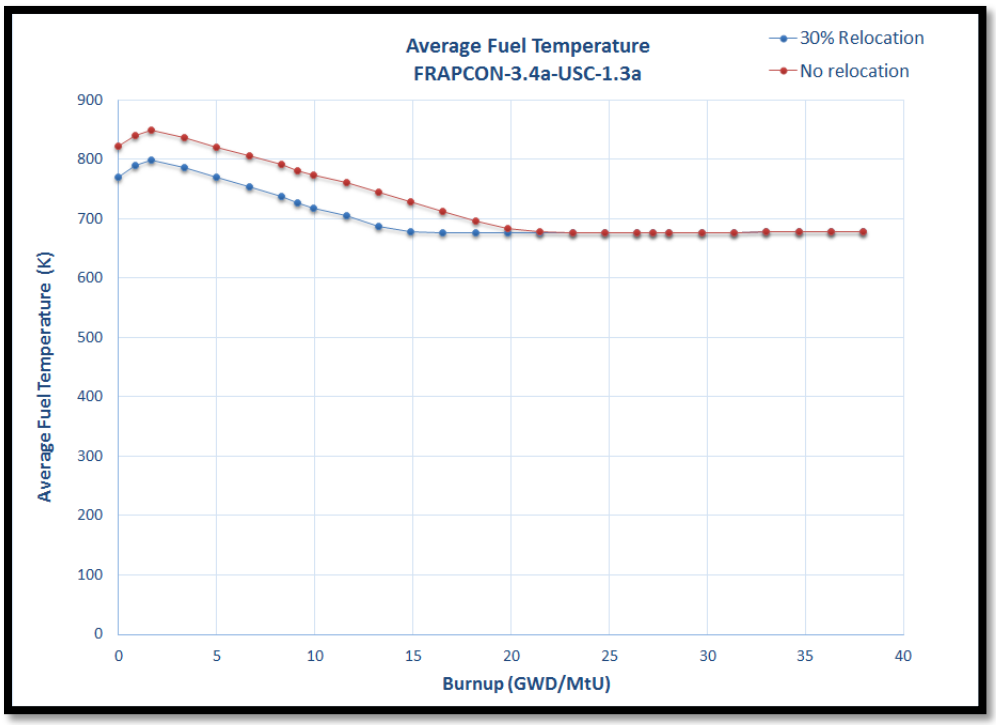

Figure 5.5 Average fuel temperature

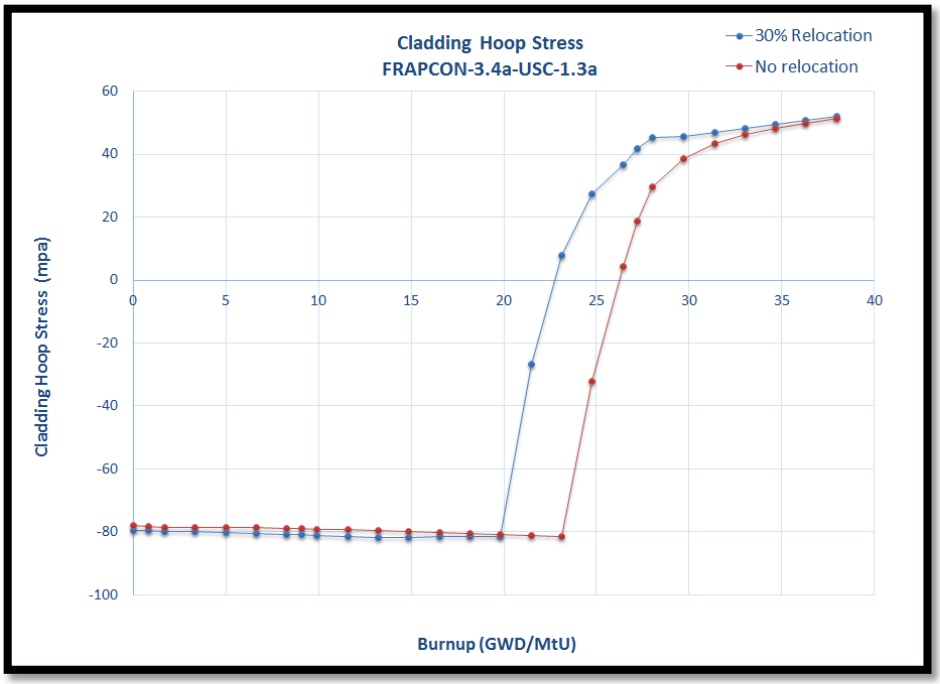

Figure 5.6 Cladding Hoop Stress

Figure 5.3 is intended to verify that relocation is occurring, which it is. The red line represents the case for which no cracking occurs, and the blue represents a case in which half of the as-fabricated gap distance has been consumed by the relocated pellet. The as-fabricated gap distance is 79 microns, and 30% relocation translates into 23.7 microns of fuel relocated into the gap; in other words, the gap is reduced to 55.3 microns.

In Figure 5.4, the structural gap is presented. Firstly, note that the gap closes significantly earlier when relocation occurs. When the structural radial gap closes, soft contact begins. At this point, one half of the relocated radius must be recovered before hard contact occurs. Hard contact in the case of relocation is also noted in the picture. Hard contact is initiated sooner because only 50% of the void volume is available to compensate fuel expansion. In the case where no relocation occurs, when contact is

made, it is 'hard contact.' The structural radial gap is dependent on both the fuel and cladding dimensional changes.

In Figure 5.5, fuel average temperatures are presented. In the case of relocation, the average fuel temperatures are 51˚C lower than that of a case in which no cracking occurs. However, as shown in Figure 5.4, contact between fuel and cladding will occur earlier because only 50% of the void volume is available for recovery.

In Figure 5.6, the cladding hoop stress is presented. The general behavior is the same in both cases; however, because hard contact occurs earlier in the case of relocation the cladding experiences contact stresses earlier.

The main conclusion that can be drawn from this is that relocation helps to lower the fuel temperatures. However, hard contact between fuel and cladding will occur earlier because only half of the initial gap volume is available to compensate fuel swelling. In a high swelling fuel like uranium carbide, where thermal conductivity is high and fuel temperatures are low, the lack of cracking may be advantageous. In other words, uranium carbide may be able to withstand a small temperature increase for a delayed contact.

5.1.6 Analysis of Implementation

After completely implementing uranium carbide into FRAPCON-3.4, a test case was performed in order to verify that the newly applied material properties and models were performing realistically. PWR conditions were used with ZIRLO as the cladding and water as the coolant. A constant power profile was employed. The specific FRAPCON input conditions can be seen in the following table.

Table 5.6 Test case between UO_2 and UC

Property	Value	
Fuel composition	UO_2	UC
Fuel enrichment (%)	4.5	4.5
Fuel theoretical density (%)	95	85
Fuel pellet type	Solid cylindrical	Solid cylindrical
Fuel pin diameter (mm)	9.144	9.144
Fuel pellet diameter (mm)	7.842	7.842
Clad thickness (mm)	0.572	0.572
Fuel height (m)	3.6576	3.6576
Coolant pressure (MPa)	15.5	15.5
Coolant inlet (K)	564.43	564.43
Coolant mass flux (kg/m^2s)	15.5	15.5
LHGR (kW/m)	18	18

In the following comparison, five graphs are presented: densification, swelling, swelling rate, thermal expansion and relocation. In FRAPCON 3.4, these are the primary contributors to fuel surface displacement. However, after soft contact, dimensional changes in the cladding also play a role.

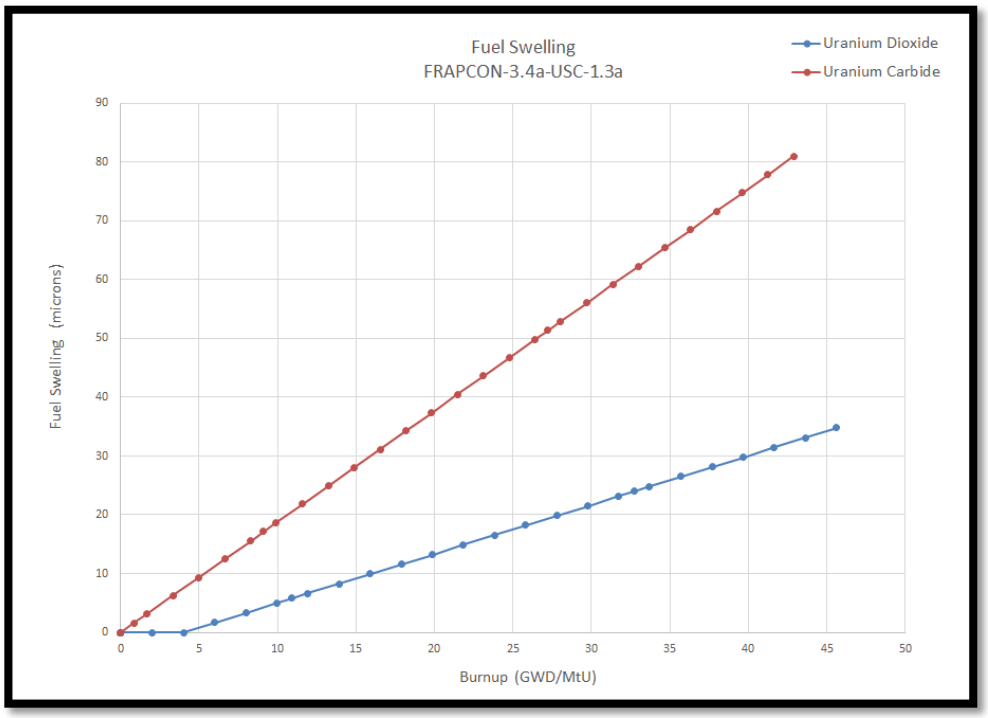

Figure 5.7 Fuel swelling in UC vs. UO_2

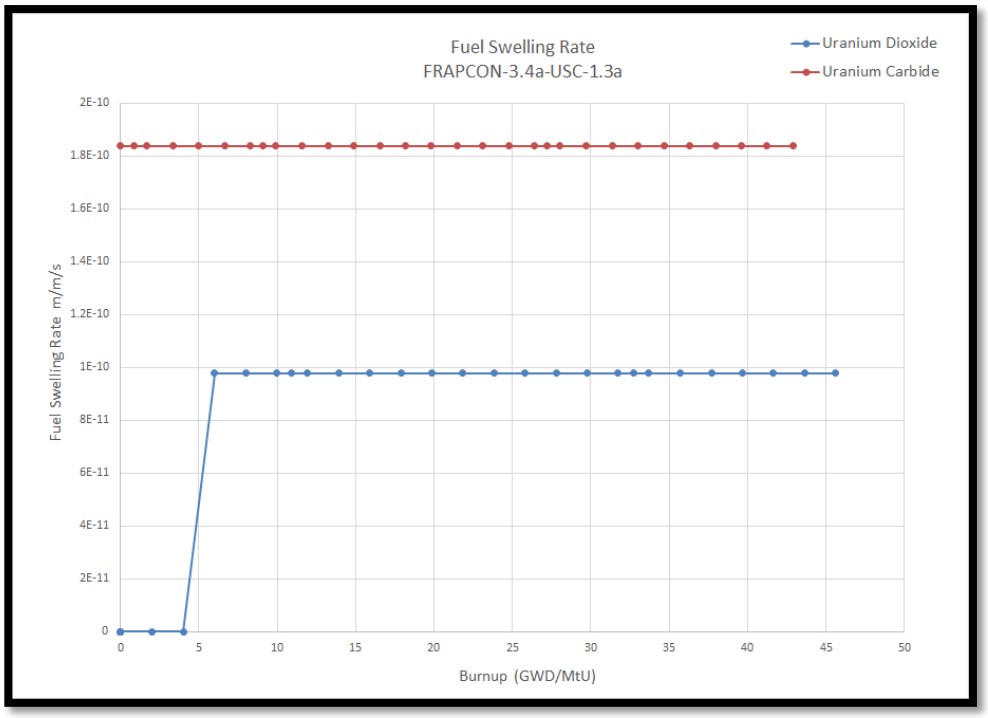

Figure 5.8 Fuel swelling rate in UC vs. UO_2

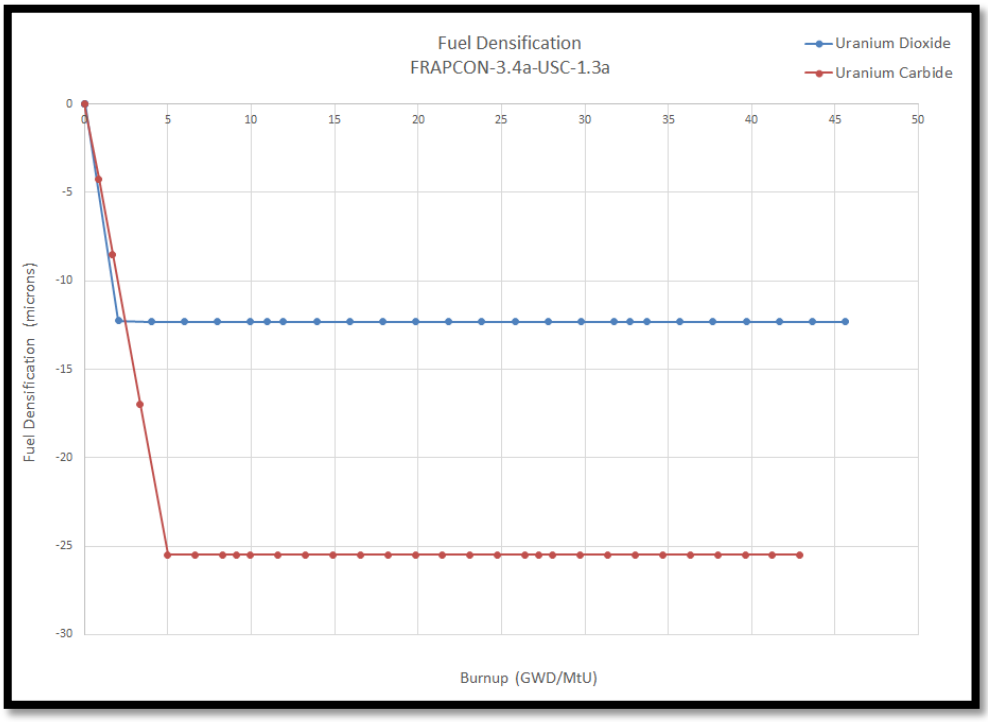

Figure 5.9 Fuel densification

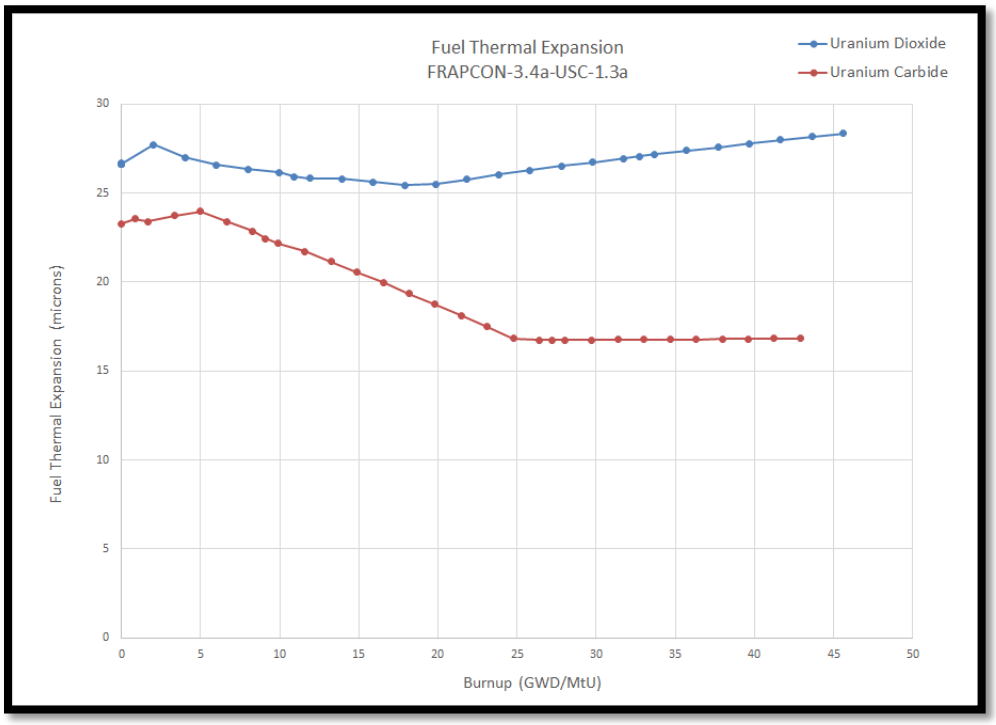

Figure 5.10 Thermal expansion in UC vs. UO_2

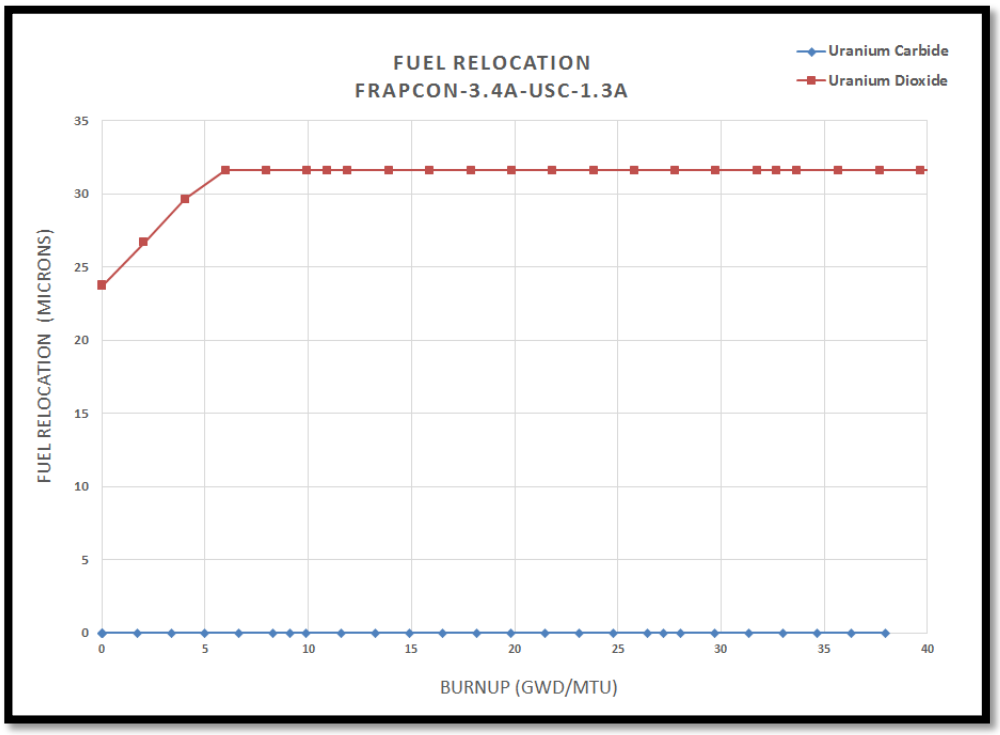

Figure 5.11 Relocation in UC and UO_2

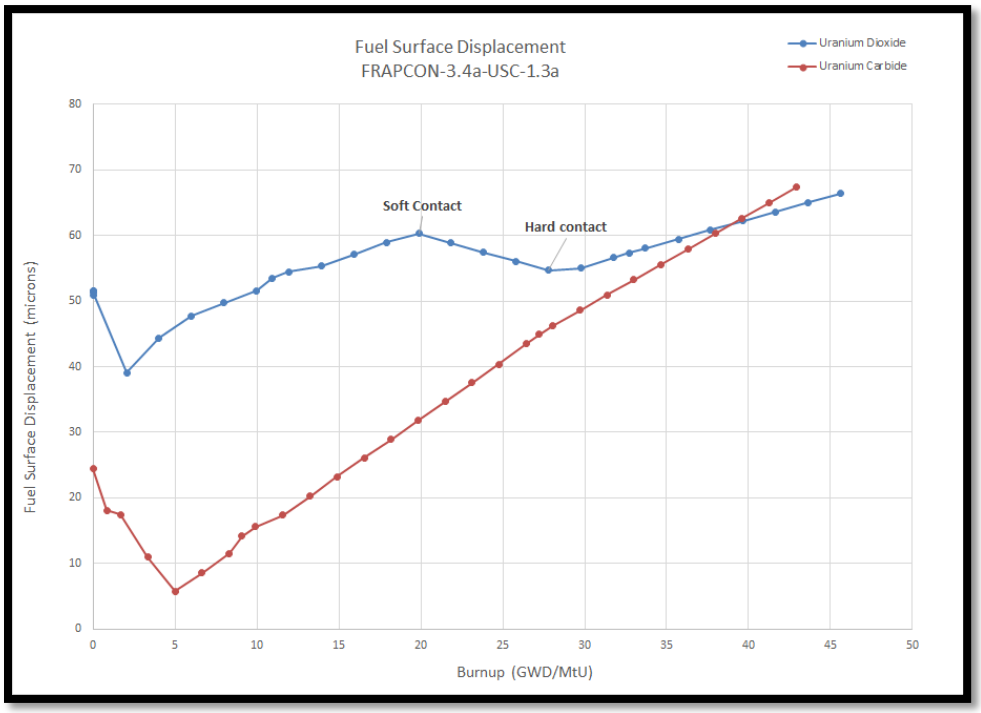

Figure 5.12 Total fuel surface displacement

In Figures 5.7, 5.8, and 5.9, fuel swelling and densification are depicted. In FRAPCON 3.4, swelling and densification are treated together. This is accomplished by delaying the onset of swelling; in other words, it is assumed that the initial fuel swelling is negated by densification. Also, 'additional densification' is calculated to account for any densification beyond that of the offset swelling amount; this is seen in Figure 5.9. For uranium carbide, swelling and densification have been treated independently. From the literature, carbides are known to swell at a rate more than twice that of uranium dioxide. The results in the figure agree well.

In Figure 5.10, thermal expansion as calculated for UO2 and UC is presented. Although UO_2 and UC have similar thermal expansion coefficients, because UC operates at a much lower temperature, thermal expansion contributes less to the fuel surface displacement. In Figure 5.11, fuel relocation is shown. Of particular importance is that UO_2 cracks where as UC does not. As a result, there is an initial gap decrease.

In Figure 5.12, the total fuel surface displacement is shown. Once UO_2 experiences soft contact, additional outward displacement is not possible until 50% of the relocated voids are recovered. The downward slope of the fuel surface displacement line can be attributed to creep of the cladding. Once 50% has been recovered, outward fuel displacement resumes; hard contact begins. UC does not experience a soft contact regime; fuel displacement is primarily dominated by swelling (once the initial densification and expansion effects have completed).

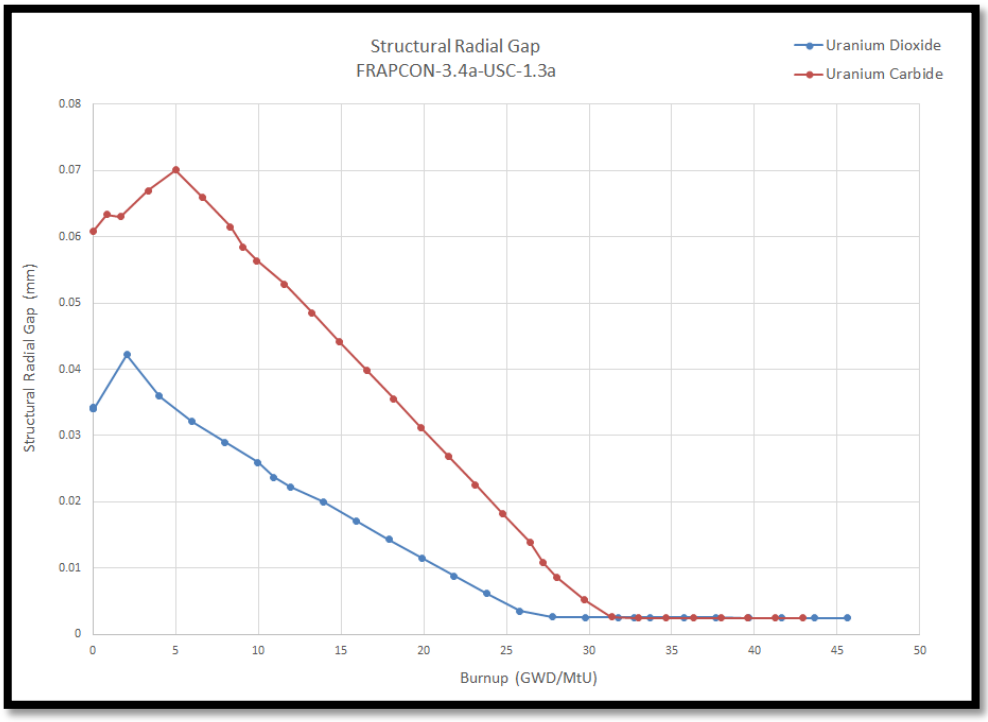

Figure 5.13 Structural radial gap

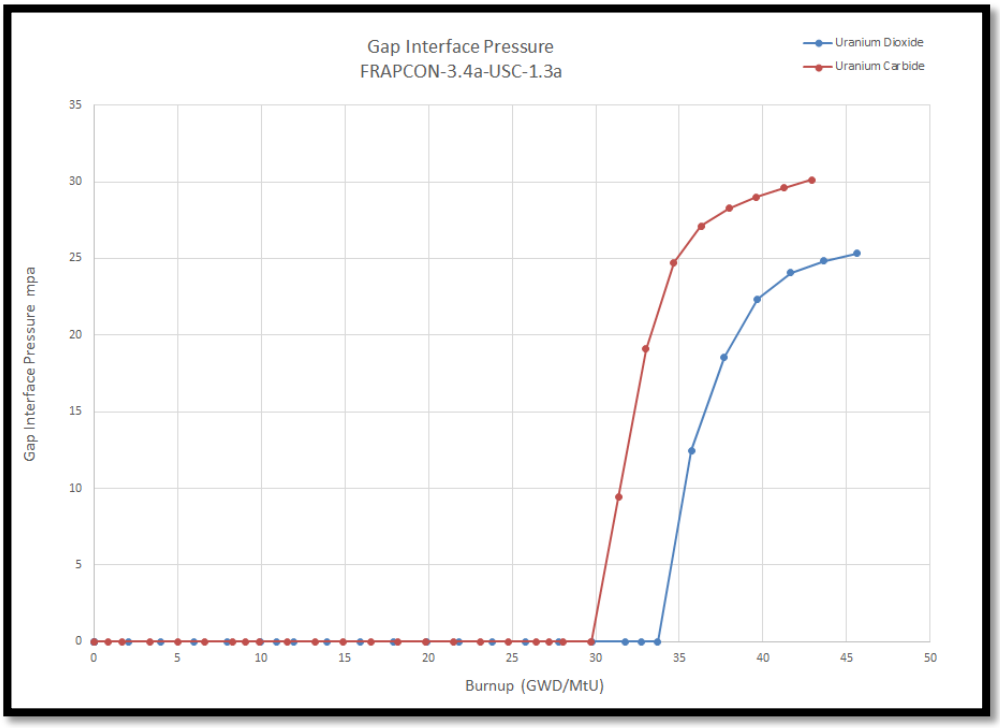

Figure 5.14 Gap interface pressure

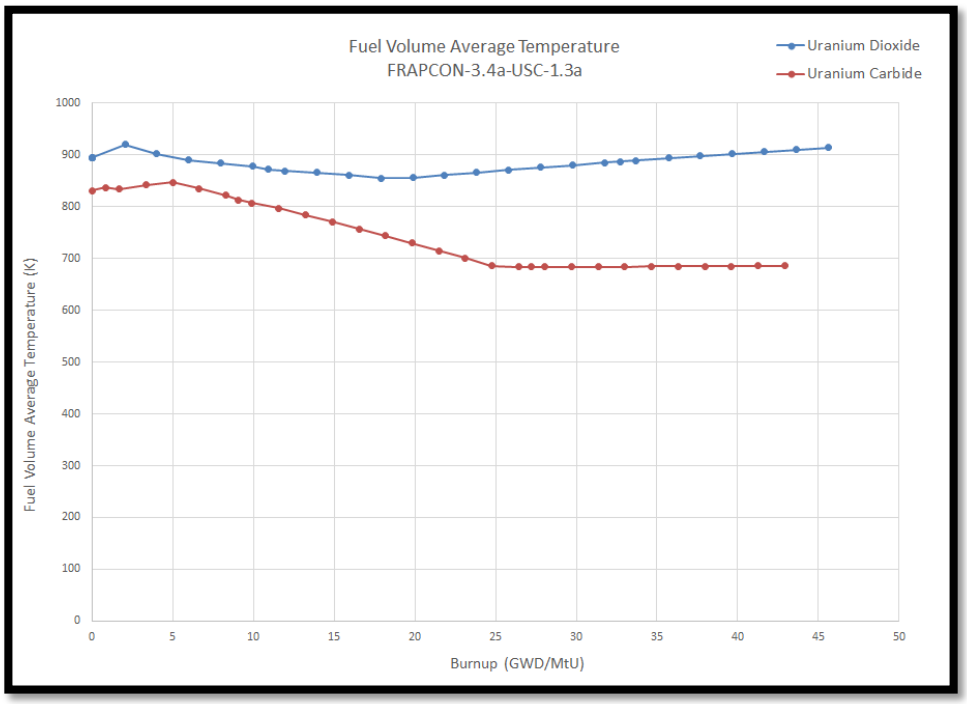

Figure 5.15 Average fuel temperature

As a result of the much higher swelling rate, the cladding is subjected to contact earlier than that of UO_2 under identical conditions. Although uranium dioxide fuel cracks and has a much smaller gap to close, notice that UC still closes the gap earlier. This results in a high interfacial pressure (~25MPa) on the cladding (Fig 5.14). Lastly, in Figure 5.14**,** the average fuel temperature is presented. Because carbide has a thermal conductivity that is five times that of oxide fuel, its operating temperatures are nearly 200 degrees less.

5.2 Implementing Helium as a Coolant

FRAPCON3.4-USC1.3 incorporates the material properties of helium gas as they are discussed in the Peterson report. FRAPCON's single channel enthalpy rise model is used to establish a bulk temperature. Forced convection is assumed to be the only means of heat conduction to the fuel rod. Additionally, oxidation and crud are set to zero.

5.2.1 Bulk Coolant Temperature Calculation

FRAPCON-3.4-USC1.3 calculates the bulk coolant temperature assuming a single, closed coolant channel enthalpy rise model. The calculation is dependent on user-supplied conditions: coolant inlet temperature (T_{in}), coolant channel equivalent heated diameter (D_0), coolant mass flux (G), and the axial heat generation rate (q"). The specific heat (C_p) of helium is taken to be constant: 5195 J/kg-K.

$$T_b(z) = T_{in} + \int_0^z \left[\frac{(\pi D_0)\, q''(z)}{C_p G A_f} \right] dz$$

5.2.2 Calculating the Rod Surface Temperature

For helium, forced-convection is assumed to be the only method of heat transfer between the coolant and cladding. Based on the work of Melese, this is an acceptable assumption under operating conditions. The McEligiot correlation for large temperature gradients was implemented to determine the Nusselt number; it is dependent on the Reynolds number (Re), Prandtl number (Pr), coolant temperature (T), rod surface temperature (T_s), and the coolant length-to-diameter (z/D) [23, 28, 29].

$$Nu = 0.021\, Re^{0.8}\, Pr^{0.4}\, (T_s/T)^{-0.5}\, [1 + (z/D)^{-0.7}]$$

Using the Nusselt number, the temperature drop at the rod surface can be determined:

$$\Delta T(z) = q'' / [(k/D_H)\, Nu]$$

5.3 Implementing Silicon Carbide

The material properties of FRAPCON3.4 have been updated to include those of silicon carbide. The following section very briefly reviews the research efforts of Bo-Shiuan Li; for a more thorough review of the physics, refer to his thesis work [32]. The properties are based primarily off the Silicon Carbide Handbook by Lance Snead and

reflect material properties associated with a high-purity β–SiC monolithic cladding that has been produced by the chemical vapor deposition method.

Table 5.7 Monolithic SiC material properties at room temperature

Material Properties	**Monolithic SiC**
Theoretical Density (g/cm^3)	3.21
Melting Temperature (K)	3000
Thermal Conductivity (W/m-K)	350
Thermal Expansion Coef (10^{-6}/K)	2.2
Elastic Modulus (GPa)	384
Yield Strength (MPa)	261 - 551
Poisson's Ratio	0.21

5.3.1 THERMAL PROPERTIES

Because FRAPCON is a steady state-code, the only thermal properties necessary to model SiC are thermal conductivity, thermal expansion, and thermal creep. Thermal conductivity was implemented as a function of temperature and burn-up. Based on experimental data, it is shown that SiC experiences a severe degradation in conductivity with increased burnup. The implemented model saturates at a value of 3.6 W/m-K at 1 DPA [14,15]. Thermal expansion is modeled as being isotropic and a function of temperature; experimental data indicates that irradiation has little effect on its behavior. Thermal creep has only been observed above 1400˚C, which is out of the scope of this research; therefore, it has been set to zero.

5.3.2 HEAT TRANSFER

For heat transfer due to hard contact between the fuel and cladding, a new cladding Meyer's hardness was implemented; it is based on the as-fabricated cladding density and temperature.

5.3.3 MECHANICAL PROPERTIES

The elastic modulus and shear modulus of silicon carbide have been added as functions of neutron fluence and temperature. Research indicates that SiC experiences a negligible amount of irradiation-induced creep, on the order of five magnitudes lower than Zircaloy. Therefore, in FRAPCON, cladding creep was set to zero. Plastic deformation has also been set to zero due to its characteristic brittle behavior; it is assumed that upon reaching yield strength, SiC will fail immediately. Lastly, due to insufficient data, it is unclear whether the cladding will oxidize; oxidation has been turned off, as well as hydrogen uptake into the cladding.

CHAPTER VI

SIMULATION OF PERFORMANCE

In the following chapter, FRAPCON3.4-USC1.3 is benchmarked against COMSOL and known data from the Fort St. Vrain reactor. COMSOL is a multiphysics-based simulation software capable of a high degree of user customization. In particular, it affords us the ability to benchmark and test a model for which little data exists. And because no known data is available for the interactive behavior of these three materials (UC, SiC, He), COMSOL is ideal. Its use grants us the capacity to not only compare the coolant conditions, but the temperature profile across the fuel for a given time and axial location with a high degree of accuracy.

6.1 FORT ST. VRAIN

In order to validate the implemented material properties, a benchmark case was performed; the input conditions were based on General Atomics' Fort St. Vrain reactor, which operated as a high temperature gas reactor from 1979 to 1989. The operating conditions are listed in **Table 6.1** [30].

Table 6.1 The operating parameters of Fort St. Vrain

	Fort Saint Vrain Operating Parameters	
	Property	**Value**
Power Conditions	Avg. Surface Heat (kW/m2)	140
	Core Power Density (MW/m3)	6.3
Coolant Conditions	Mass Flow (kg/s)	453
	Flow Area (m2)	4.738
	Mass Flux (kg/s-m2)	94.1
	Pressure (MPa)	4.8
	Inlet Temperature (˚C)	405
	Outlet Temperature (˚C)	775
	Temperature Rise (˚C)	370

The dimensions below were used for the fuel geometry; they are based on a typical PWR fuel rod with the exception of core length, which was taken from Fort St. Vrain. The performance parameters listed in **Table 6.1** were scaled to accommodate the geometry below. The Fort St. Vrain coolant flow area was taken as an average of the fuel element (despite its varying coolant channel sizes). See **Figure 6.1**. and **Figure 6.2.**

Table 6.2 Input for FRAPCON & COMSOL benchmark

	FRAPCON Input	
	Property	**Value**
Geometry	Cladding Diameter (m)	0.008
	Fuel Diameter (m)	0.008
	Cladding Thickness (m)	0.000572
	Fuel Rod Pitch (m)	0.01335709
	Active Fuel Rod Height (m)	4.758
Heat Generation	Surface Heat (MW/m3)	80
	Volumetric Heat (kW/m2)	140
	Linear Heat Flux (kW/m)	4.022
Coolant Conditions	Mass Flux (kg/s-m2)	94.1
	Pressure (MPa)	4.8
	Channel Flow Area (m2)	9.86374E-05
	Inlet Temperature (˚C)	405

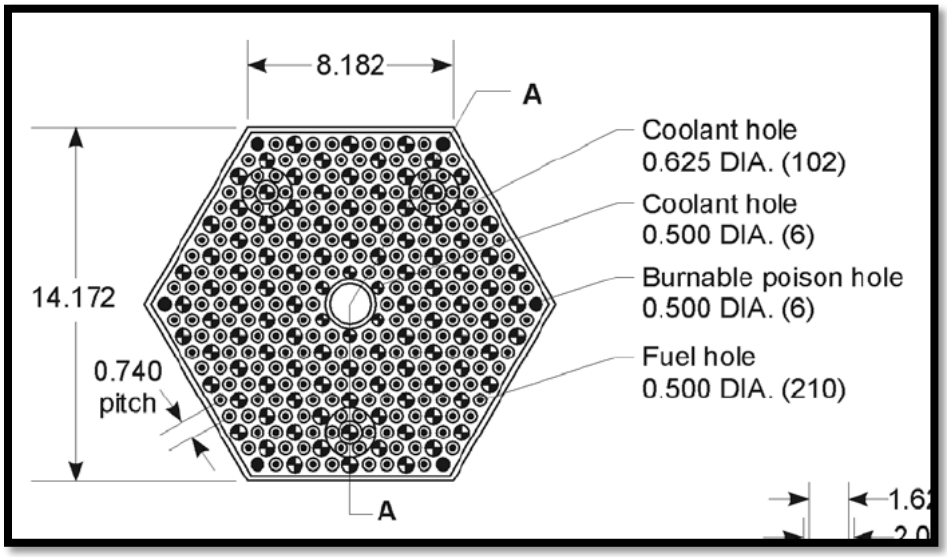

Figure 6.1 FSVR fuel element

Table 6.3 FSVR Fuel element characteristics

Characteristics	Control Element	Bottom Control Element	Standard Element
Approximate Weight (with fuel compacts/matrix, kg)	109	111	128
Graphite body (kg)	85	94	86
Number of coolant holes (12.700 mm and 15.875 mm dia.)	57	57	108
Number of Fuel Holes (12.70 mm dia.)	120	120	210
Fuel Hole Pitch (mm)	18.796	18.796	18.796
Number of Control Rod Drive Holes (101.60 mm dia.)	2	2	0
Number of Reserve Shutdown Holes (95.25 mm)	1	1	0

6.2 Coolant Temperature Calculation

Using the Fort St. Vrain operating parameters above, a benchmark case was performed with FRAPCON3.4-USC1.3 and COMSOL. Of primary interest for this simulation is the bulk coolant temperature calculation. The purpose of this preliminary exercise is to determine the validity of the implemented properties and physics.

Figure 6.1 below depicts the predicted temperature rise through the coolant channel. The literature indicates that Fort St. Vrain experiences an average temperature rise of 370˚C. By comparison, FRAPCON3.4-USC1.3 predicted a temperature increase of 345˚C and COMSOL predicted a temperature increase of 330˚C.

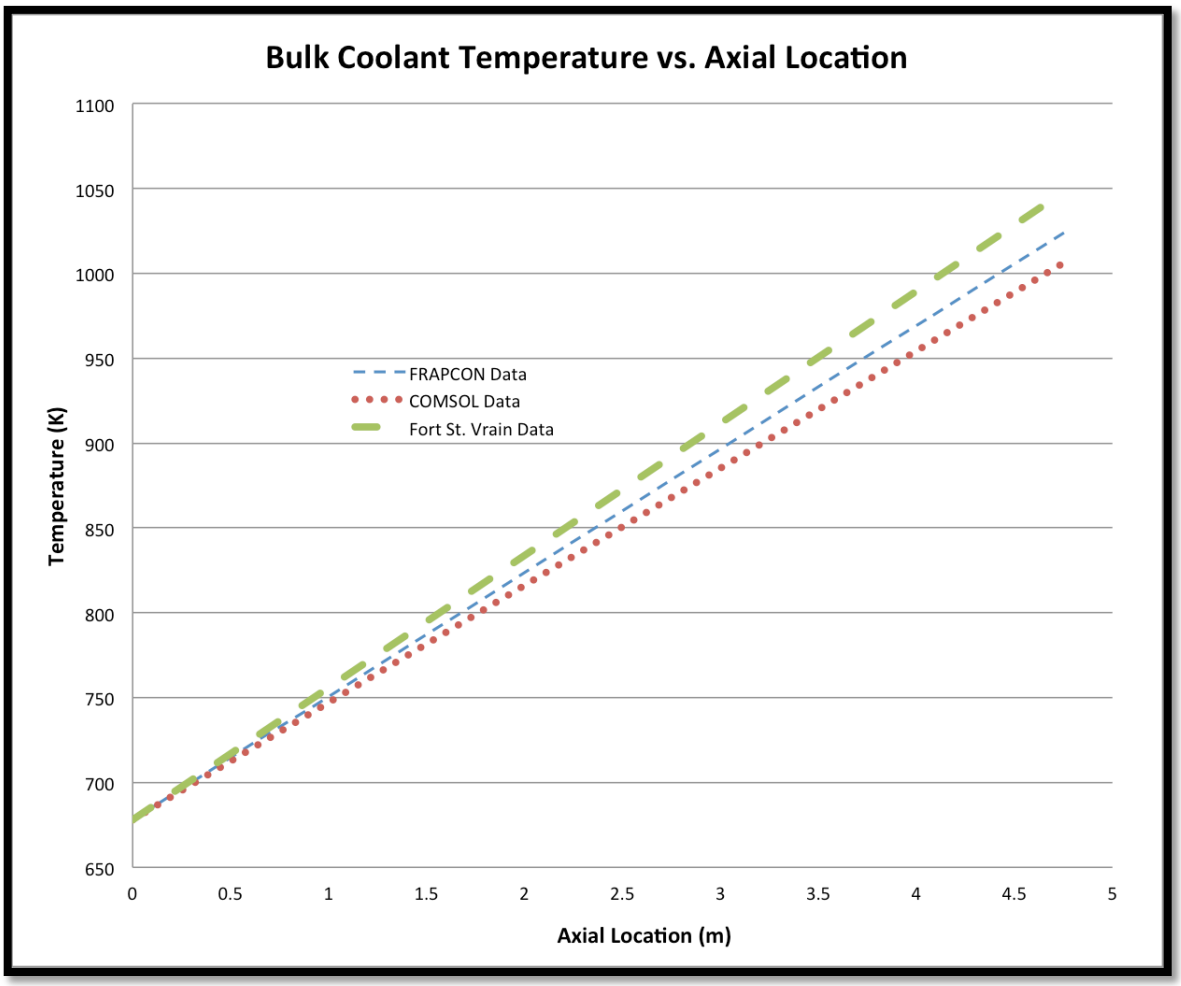

Figure 6.1 Comparison of bulk coolant calculation

A comparison of the COMSOL and FRAPCON-USC results with the Fort St. Vrain data indicates that a relatively small percent difference exists between them. A degree of error may be attributed to the Fort St. Vrain data itself. However, the results agree well enough and suggest the model is performing reasonably.

Perhaps more indicative of the reliability of the FRAPCON model are the COMSOL results. A comparison between the two cases reveals a smaller percent difference. This result indicates that the model has been implemented appropriately and is returning a value within reason.

Table 6.4 Percent difference between methods

Comparison	Difference (%)
Fort St. Vrain / FRAPCON-USC1.3	6.99
Fort St. Vrain / COMSOL	11.4
FRAPCON-USC1.3 / COMSOL	4.44

6.3 Fuel Rod Temperature Profile

The use of COMSOL grants us the capacity to not only compare the coolant conditions, but the temperature profile across the fuel for a given time and axial location. Due to the novel nature of the research, experimental data is scarce. COMSOL affords us the ability to verify and validate the chosen physics.

In the following example, the input conditions are the same as the previous case. A test case was executed with FRAPCON3.4-USC1.3. Then, at the point of initial contacts, the FRAPCON output was reviewed; it was used as input conditions for COMSOL. The intention is to replicate the same scenario.

At the chosen time step, the fuel has come into contact with the cladding, i.e. the fuel-clad gap is zero. The following images are captured at an axial height of 4.75 meters (outlet position). Constant power conditions over the length of the rod were used in both scenarios.

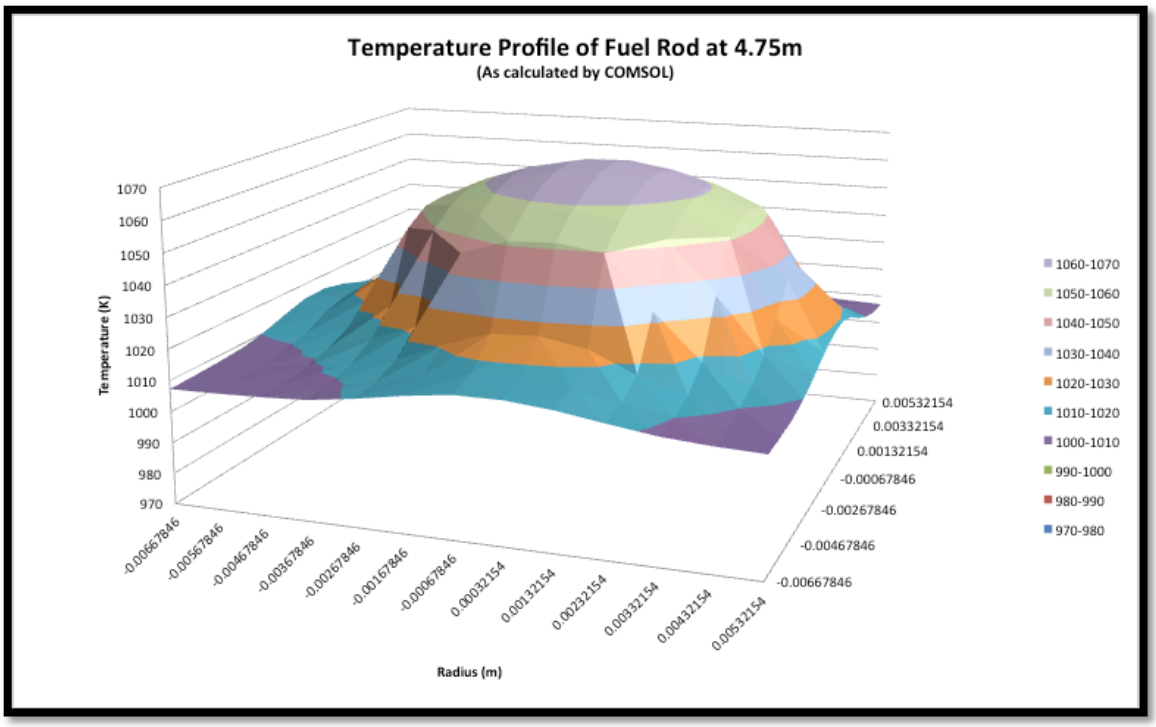

Figure 6.2 Temperature profile of fuel rod channel

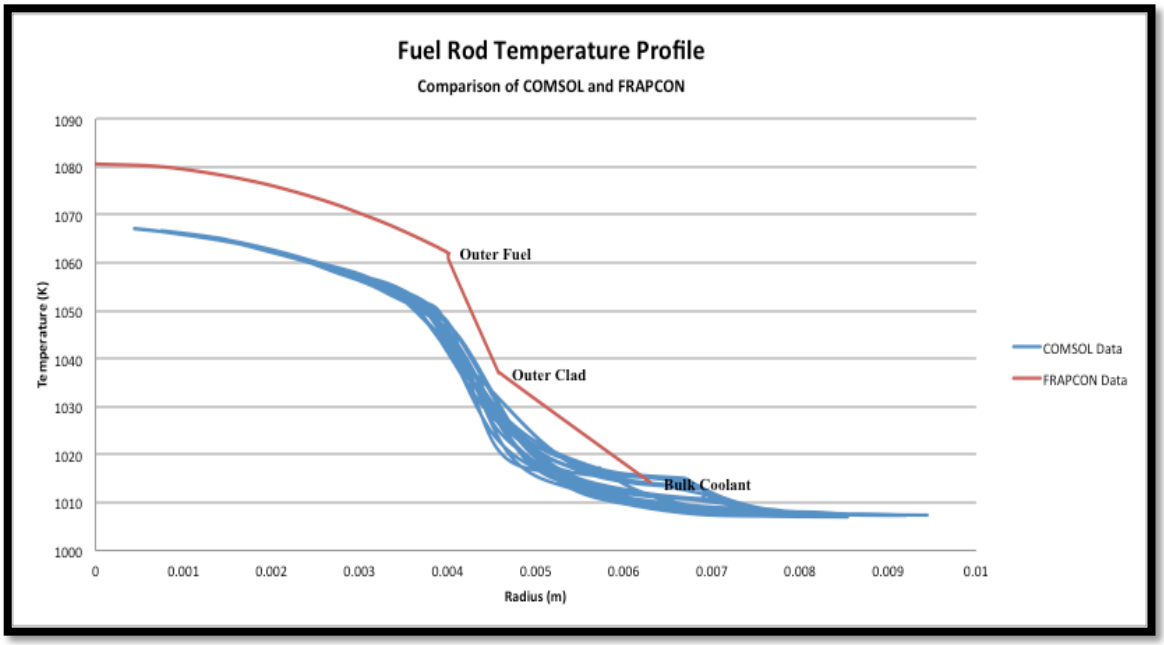

Figure 6.3 Temperature profile across fuel rod

Again, the preliminary FRAPCON results agree well with those calculated by COMSOL. The USC1.3 model predicted a slightly higher fuel temperature profile than that of COMSOL, however the general behavior agrees well with COMSOL. It's worth noting that the temperature profile experienced only a 56-degree Celsius temperature gradient, however this is only due to the extremely low LHGR, which was used to replicate equivalent heat conditions in the fuel rod channel. Much higher linear heat generation rates are to be expected.

CHAPTER VII

CONCLUSIONS

Uranium carbide has shown considerable promise as a nuclear fuel because of its high uranium density, good irradiation stability, and especially high thermal conductivity. However, carbide's swelling behavior is the root of many concerns, especially when paired with a brittle ceramic like that of silicon carbide.

To better understand the interaction between these advanced materials, each material was implemented into FRAPCON 3.4, the preferred fuel performance code of the NRC; additionally, the material properties and the heat transfer physics associated with a gas coolant were incorporated. The implementation of carbide within FRAPCON required the development of material models that described not only the thermophysical properties of UC, such as thermal conductivity and thermal expansion, but also models for the swelling, densification, and fission gas release associated with the fuel's irradiation behavior.

The currently implemented models associated with FRAPCON3.4-USC1.3 are based on the limited experimental data that is available. In most cases, the effects of stoichiometry and composition are unaccounted for. Further data is necessary in order to refine the material properties associated with UC. Additionally, emphasis should be placed on the effects of carbide cracking, i.e. relocation and recovery. Understanding

these phenomena is absolutely critical to adequately determine the PCMI behavior of UC and SiC.

REFERENCES

[1] WORLD NUCLEAR ASSOCIATION. 2010. Generation IV Nuclear Reactors. World Nuclear Association. Available: http://www.world-nuclear.org/info/Nuclear-Fuel-Cycle/Power-Reactors/Generation-IV-Nuclear-Reactors/

[2] ABRAMS B., LEVY S. & CHAPIN D. 2002. A technology roadmap for generation IV nuclear energy systems. US DOE Nuclear Energy Research Advisory Committee and the Generation IV International Forum. Available: http://www.gen-4.org/PDFs/GenIVRoadmap.pdf

[3] ANZIEU P., STAINSBY R. & MIKITYUK K. 2009. Gas-cooled fast reactor (GFR): overview and perspectives. *Paris, France 9-10 September 2009* 127.

[4] O'CONNOR T.J. 2009. Gas Reactors–A Review of the past, an Overview of the Present and a View of the Future. GIF Symposium, Paris (France): 9-10.

[5] GENERAL ATOMICS. 2013. Energy Multiplier Module. Available: http://www.ga.com/energy-multiplier-module

[6] PARMENTOLA J. 2010. Energy Multiplier Module. Available: http://www.ga.com/energy-multiplier-module

[7] CHOI H., SCHLEICHER R.W. & GUPTA P. A Compact Gas-Cooled Fast Reactor with an Ultra-Long Fuel Cycle. *Science and Technology of Nuclear Installations*. Volume 2013

[8] PEAKALL K.A. & ANTILL J.E. 1962. Oxidation of uranium monocarbide. *Journal of the Less Common Metals*

[9] FROST B.R.T. 1963. The carbides of uranium. *Journal of Nuclear Materials* 10: 265-300.

[10] JONES R.W. & CROSTHWAITE J.L. 1973. Uranium Carbide Fuel for Organic Cooled Reactors. *Atomic Energy of Canada Limited, Rep. AECL-4443*

[11] BLANK H. 1994. Nonoxide ceramic nuclear fuels. *Materials science and technology*

[12] ROUGH F.A. & DICKERSON R.F. 1960. Uranium Monocarbide – Fuel of the Future. *Nucleonics (US) Ceased publication* 18

[13] NICKERSON G.M. & KASTENBERG W.E. 1976. Preliminary assessments of carbide fuel pins during mild overpower transients in LMFBRs. *Nuclear Engineering and Design* 36: 209-233.

[14] LEWIS H.D. & KERRISK J.F. 1976. Electrical and thermal transport properties of uranium and plutonium carbides.

[15] PREUSSER T. 1982. Modeling of carbide fuel rods. *Nuclear Technology; (United States):* 57

[16] DE CONINCK R., VAN LIERDE W. & GIJS A. 1975. Uranium carbide: Thermal diffusivity, thermal conductivity and spectral emissivity at high temperatures. *Journal of Nuclear Materials* 57: 69-76.

[17] WASHINGTON A.B.G. 1973. *Preferred values for the thermal conductivity of sintered ceramic fuel for fast reactor use*. HM Stationery Office.

[18] KRIKORIAN O.H. 1960. Thermal expansion of high temperature materials.

[19] CRANE J. & GORDON E. 1964. The Development of Uranium Carbide as a Nuclear Fuel. *United Nuclear Corporation report UNC-5080*

[20] MENDEZ-PENALOSA R. & TAYLOR R.E. 1964. Thermal Expansion of Uranium Monocarbide. *Journal of the American Ceramic Society* 47: 101-102.

[21] RICHARDS H.K. 1971. Thermal Expansion of Uranium and Tantalum Monocarbides up to 2700 C. *Nuclear Technology* 10: 54-61.

[22] DIENST W. 1984. Swelling, densification and creep of (U, Pu) C fuel under irradiation. *Journal of nuclear materials* 124: 153-158.

[23] MELESE G. & KATZ R. 1984. Thermal and flow design of helium-cooled reactors.

[24] PETERSEN H. 1970. The properties of helium: density, specific heats, viscosity, and thermal conductivity at pressures from 1 to 100 bar and from room temperature to about 1800 K.

[25] OGUMA M. 1983. Cracking and relocation behavior of nuclear fuel pellets during rise to power. *Nuclear engineering and design* 76: 35-45.

[26] GEELHOOD K.J., W.G. LUSCHER & C.E. BEYER 2011. *FRAPCON-3.4: A Computer Code for the Calculation of Steady State Thermal-mechanical Behavior of Oxide Fuel Rods for High Burnup*. US Nuclear Regulatory Commission, Office of Nuclear Regulatory Research.

[27] GEELHOOD K.J., LUSCHER W.G., SENOR D.J., CUNNINGHAM M.E., LANNING D.D. & ADKINS H.E. 2009. Predictive Bias and Sensitivity in NRC Fuel Performance Codes.

[28] MCELIGOT D.M., MAGEE P.M. & LEPPERT G. 1965. Effect of large temperature gradients on convective heat transfer: The downstream region. *Journal of Heat Transfer* 87: 67.

[29] MCELIGOT D.M., MCCREERY G.E., SCHULTZ R.R. & LEE… J. 2006. Investigation of Fundamental Thermal-Hydraulic Phenomena in Advanced Gas-Cooled Reactors. *inl.gov*

[30] CHOI H., SCHLEICHER R.W. 2011. Design Characteristics of the Energy Multiplier Module (EM^2). *Transactions of the American Nuclear Society.* 104: 929-930.

[31] GEELHOOD K.J., LUSCHER W.G.,, *Material Property Correlations: Comparisons between FRAPCON-3.4, FRAPTRAN 1.4, and MATPRO* (US Nuclear Regulatory Commission, Office of Nuclear Regulatory Research, 2011).

[32] LI, B. 2013. Pellet Cladding Mechanical Interactions of Ceramic Claddings Fuels Under Light Water Reactor Conditions.